Acta Mech 230, 1105–1128 (2019)
https://doi.org/10.1007/s00707-018-2336-7

ORIGINAL PAPER

Alessandra Genoese · Andrea Genoese · Ginevra Salerno

On the nanoscale behaviour of single-wall C, BN and SiC nanotubes

Received: 25 July 2018 / Revised: 9 November 2018 / Published online: 2 January 2019

Abstract The paper presents a numerical study of defect-free single-wall carbon, boron nitride and silicon carbide armchair and zigzag nanotubes, through a simple stick-and-spring model, based on Morse and cosine potential functions. The study investigates the relaxed configuration of the tubes and gives a comprehensive evaluation of their elastic constants, which is performed by framing tensile, torsional and radial tests within the membrane behaviour of a Donnell thin shell model. Extensive comparisons with reference ab-initio results are given and used to refine some parameters of the potential functions for hexagonal silicon carbide nanomaterials.

1 Introduction

Over the last two decades, interest in the applications of graphene and carbon nanotubes (CNTs) has continuously grown in a variety of fields, including microelectronics, sensoring and actuation systems, energy storage, biotechnologies and composite materials [1–7]. In parallel, many researchers have also investigated nanomaterials consisting of elements other than carbon (C), including boron (B), nitrogen (N) and silicon (Si). Some examples are boron nitride and silicon carbide nanosheets and the related nanotubes (BNNTs, SiCNTs) [8–12]. Similarly to their C analogues, these nanomaterials exhibit exceptional thermo-mechanical properties, such as low density and high thermal conductivity [13–19]. Moreover, the different atomic composition leads to some specific properties, such as stronger resistance to oxidation and chemical stability at high temperatures, giving them advantages over C nanomaterials in harsh environments [13,17–19]. As of now, these nanomaterials have drawn attention in different technological fields, including the manufacture of semiconductors [13,20] (e.g. BN/graphene heterostructures for electronic devices) and hydrogen storage [21]. In addition, BN compounds can also be cleaned and reused by means of heating and burning in air, are biocompatible, have low friction coefficient, have excellent sorption performance and are hydrorepellent. For these reasons, they are studied also for applications in medicine (e.g. drug delivery), as lubricants and for water purification from oil, solvents and dyes [17–19].

The control of the mechanical behaviour of nanomaterials is a key challenge in the design of their composites and in many other contexts, such as nanosensors, nanoresonators, selective membranes and flexible nanoelectronics [22–24]. In this regard, it is also emphasizing worth that the deformation influences the

Alessandra Genoese (✉) · Andrea Genoese · G. Salerno
LiMES, Dipartimento di Architettura, Università Roma Tre, Via Madonna dei Monti 40, 00184 Roma, Italy
E-mail: alessandrag_83@hotmail.it

Andrea Genoese
E-mail: andreagenoese_83@hotmail.it

G. Salerno
E-mail: ginevra.salerno@uniroma3.it

chemical–physical properties of any material at the nanoscale. Tuning these properties in specific devices through deformation control is therefore possible, in principle.

Due to the technical difficulties and the costs of nanoscale experiments (e.g. [14,15,25]), theoretical modelling is essential. In this regard, ab-initio simulations (e.g. [26–40]) are the most accurate tools to investigate the behaviour of nanomaterials, including their mechanics. In the last years, ab-initio simulations have given a valuable characterization of the relaxed configuration (i.e. the self-equilibrated configuration), and of some fundamental mechanical properties, such as the tensile stiffness and strength of these nanomaterials. However, ab-initio simulations demand a lot of computer power, and so they are not always feasible for systems with very many atoms. Therefore, many researchers have shifted their focus towards other approaches, such as molecular dynamics/statics formulations [41–78] and their structural–mechanical approximations (e.g. nanoscale equivalent beam and truss models) [79–85] or continuum models [86–94]. Most of this research addresses graphene and CNTs. This has produced a certain knowledge about their mechanics, also in ambitious nonlinear contexts, such as fracture [45,46,70,75,80] or buckling [47,53,57,62,88,94]. It has additionally produced a refinement of the parameters of simple bonding potentials [41,67,75,77], such as the DREIDING, the Stillinger–Weber or the modified Morse potentials. Currently, these potentials are considered to be the best compromise for describing graphene and CNTs at the atomic scale, also in nonlinear contexts, where the simplicity of the models is a major requirement.

Much less is known about BN and SiC nanomaterials, even in the linear range. In the case of tubes, even the elastic constants have not been sufficiently studied. In fact, the works in this field are very few [27,34,40,43,49–51,60,64,65] and frequently they present only partial results. As of now, for SiCNTs there exist only results about longitudinal Young modulus [34,60], while for BNNTs only the paper by Yan and Liew [65] has provided a comprehensive set of elastic constants (Young and shear moduli and Poisson ratios), but there are no considerations about possible anisotropies. Also the parameterization of the interatomic potential has not received sufficient attention. There are some parameterizations of the Tersoff–Brenner potential [43,49,95], but little has been done on the parameters of simpler interatomic potentials. In this regard, there are only the refinements of the force constants proposed by Jiang and Guo in [50] and in our previous work [74]. However, to obtain the general assessment of these parameters, which is currently lacking, it is the authors' opinion that extensive study in different contexts is necessary.

Towards this end, this paper presents a numerical study of defect-free single-wall armchair and zigzag CNTs, BNNTs and SiCNTs of several diameters through a stick-and-spring model, based on Morse and cosine potential functions [96]. CNTs are taken into account, mainly for comparison reasons.

This study investigates the relaxed configuration of tubes and gives a comprehensive evaluation of the elastic constants (surface Young and shear moduli and Poisson ratios), which is performed by framing tensile, torsional and radial tests within the membrane behaviour of a Donnell thin shell model. Extensive comparisons with reference ab-initio results are addressed. In the light of these comparisons, a refinement of the angular force constants for SiC hexagonal nanomaterials given in [74] is proposed.

We also give a detailed discussion of the stick-and-spring model. In addition, some space is given to discussing small-scale effects specific to the diatomic tube behaviours, which add to those discussed in [78] for the CNTs.

2 The stick-and-spring model of diatomic nanotubes

In this section, the atomistic model of a diatomic nanotube is discussed. The model is formulated in finite kinematics and makes use of Morse and cosine potential functions. For the purposes of the paper, the model linearization is also given. CNTs are recovered as a particular case of the diatomic tube, namely when the atoms are all of the same type.

2.1 The atomic structure and the interatomic potential

Heuristically, single-wall diatomic nanotubes can be imagined as hollow cylinders, obtained by rolling up a planar hexagonal sheet consisting of two different atom types, as depicted in Fig. 1. The sheet is assumed to be stress-free. Therefore, r_e and $\theta_e = 2/3\pi$ (see Fig. 1) are the resting bond length and angle.[1]

[1] In molecular mechanics models, the bond length is the distance between the nuclei of two first neighbouring atoms i and j, while the bond angle is defined by two pairs i–j and i–k of first neighbouring atoms.

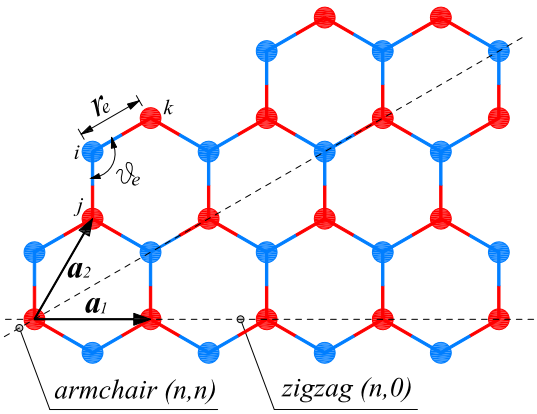

Fig. 1 Hexagonal diatomic sheet. Blue and red balls identify the type of atom 1 and 2, respectively (color figure online)

Having fixed two lattice vectors $\boldsymbol{a}_1$ and $\boldsymbol{a}_2$ as in Fig. 1, the key geometric ingredient of the tube is the chiral vector $\boldsymbol{\chi} = n\boldsymbol{a}_1 + m\boldsymbol{a}_2$, where n and m are two integers. Its modulus gives the circumference of the tube. Therefore, the pair (n, m) sorts both the radius ϱ and the way to roll the sheet or, in other words, the chirality of the tube. It is not difficult to derive that

$$\varrho = \frac{r_e}{2\pi}\sqrt{3(n^2 + m^2 + nm)}. \tag{1}$$

As for the chirality, a nanotube is said to be

1. of zigzag type if $n \neq 0$ and $m = 0$;
2. of armchair type if $n = m \neq 0$;
3. of chiral type if $n \neq m$ with $n \neq 0$ and $m \neq 0$.

In this work, only zigzag and armchair tubes are considered. As examples, the geometries of a (4, 0) and a (2, 2) diatomic tube are depicted in Fig. 2.

Given (n, m) and a length ℓ, the coordinates of the atoms are obtained by means of a conformal mapping. Letting (O, ξ, η) and (O, x, y, z) be Cartesian frames with origin in the centre of the original sheet and in the centre of the tube (see Fig. 2), the coordinates of the ith atom are given by

$$x_i = \varrho \cos\frac{\xi_i}{2\pi\varrho}, \quad y_i = \varrho \sin\frac{\xi_i}{2\pi\varrho}, \quad z_i = \eta_i. \tag{2}$$

As we can easily see, the map preserves only the atomic distances along the tube axis. Therefore, in general, the bond lengths and angles are not the same as in the sheet. Due to these changes, the tube geometry is not stress-free. This configuration is known as "ideal", since it is not necessarily in equilibrium. On the other hand, the self-equilibrated configuration is called "relaxed".

Now, let us focus on the interaction between the atoms. They are divided into bonding interactions and long-range interactions and they are mathematically described by the interatomic potential. Long-range interactions are deemed less significant than the bonding ones and are usually neglected in the models of single-wall nanotubes. Amongst the bonding interactions, we consider only the binary and ternary ones, related to the variations of the bond lengths and of the bond angles with respect to their resting state. Following [96], the interatomic potential is given by

$$U = \sum_b U_{\mathrm{b}}^r + \sum_a U_{\mathrm{a}}^\theta. \tag{3}$$

In Eq. (3), U_{b}^r and U_{a}^θ are the contributions related to the bth bond length variation and to the ath bond angle variation, respectively. They are described using the following Morse and cosine energy functions

$$U_{\mathrm{b}}^r = D\left\{\left[1 - \mathrm{e}^{-\beta(r_{ij} - r_e)}\right]^2 - 1\right\}, \tag{4a}$$

$$U_{\mathrm{a}}^\theta = A\left[1 - \cos\left(3\theta_{ijk}\right)\right]. \tag{4b}$$

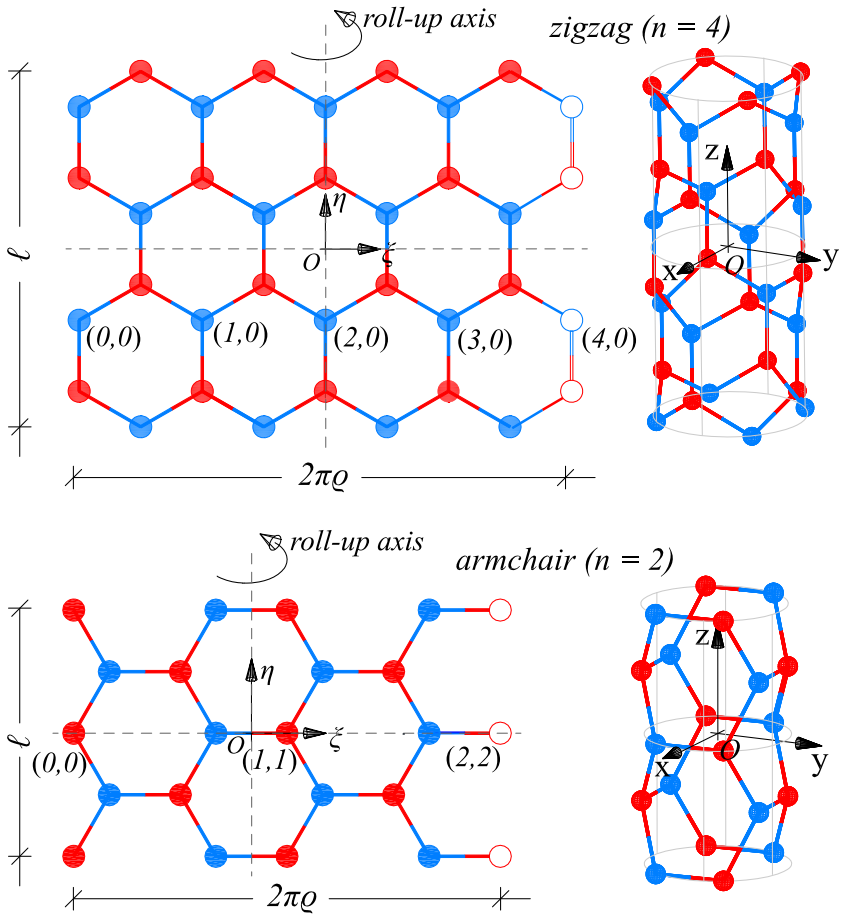

Fig. 2 An example of zigzag and armchair tube

In Eq. (4), r_{ij} is the bond length between the first neighbours i–j, θ_{ijk} is the bond angle defined by the two pairs of first neighbours i–j and i–k, D is the well depth (i.e. the minimum value of U_{b}^{r}, reached at $r_{ij} = r_e$), corresponding to the bond breaking energy, while β and A are two parameters, which will be defined later.

From the point of view of structural mechanics, Eq. (4) represents the potentials of uncoupled stick elements, endowed with axial deformation, and rotational spring elements, acting in the planes defined by the two stick elements they are attached to.

The inner forces and couples are described by the following constitutive relationships:

$$f_{ij} = \frac{\mathrm{d}U_{\mathrm{b}}^{r}}{\mathrm{d}r_{ij}} = 2D\beta\left[1 - \mathrm{e}^{-\beta(r_{ij}-r_e)}\right]\mathrm{e}^{-\beta(r_{ij}-r_e)}, \tag{5a}$$

$$m_{ijk} = \frac{\mathrm{d}U_{a}^{\theta}}{\mathrm{d}\theta_{ijk}} = 3A\sin(3\theta_{ijk}), \tag{5b}$$

which vanish at $r_{ij} = r_e$ and $\theta_{ijk} = \theta_e$. Then, the tangent stiffnesses of these elements are given by

$$k_{ij} = \frac{\mathrm{d}f_{ij}}{\mathrm{d}r_{ij}} = 2D\beta^2\left[2\mathrm{e}^{-\beta(r_{ij}-r_e)} - 1\right]\mathrm{e}^{-\beta(r_{ij}-r_e)}, \tag{6a}$$

$$k_{ijk} = \frac{\mathrm{d}m_{ijk}}{\mathrm{d}\theta_{ijk}} = 9A\cos(3\theta_{ijk}). \tag{6b}$$

Finally, for what follows, it is useful to briefly discuss the relationships between D, β and A, and the force constants, k_r and k_θ, for bond stretching and angle variation, which read

$$k_r = k_{ij}[r_{ij} = r_e] = 2D\beta^2, \tag{7a}$$

$$k_\theta = k_{ijk}[\theta_{ijk} = \theta_e] = 9A. \tag{7b}$$

These equations can be used to evaluate β and A, once D, k_r and k_θ are given. For diatomic hexagonal nanomaterials all binary interactions involve one atom of type 1 and one atom of type 2, and so they are described by the same k_r and the same D. Instead, following [96], the ternary interactions require a diversification of the force constant k_θ, depending on whether the pairs of first neighbours i–j and i–k share the atom of type 1, or the atom of type 2. We call the constants related to the two cases $\mathcal{K}_1$ and $\mathcal{K}_2$, respectively. For CNTs, the force constants $\mathcal{K}_1$ and $\mathcal{K}_2$ are equal.

2.2 The structural mechanics formulation

We now provide the kinematic compatibility equations and the equilibrium equations of the model.

2.2.1 Kinematics

The kinematic variables of the stick-and-spring model are the atom displacements, regarded as point particles in Euclidean space. The objective now is to express r_{ij} and θ_{ijk} in terms of these displacements, with $r_{ij} > 0$ and $0 < \theta_{ijk} < \pi$. To this end, we denote by $\mathbf{x}_n$ the position of the nth atom in the reference configuration (for instance, the ideal one or the relaxed one), while $\boldsymbol{u}_n$ and $\boldsymbol{p}_n$ denote its displacement and applied load. The current position of the atom is then $\boldsymbol{x}_n = \mathbf{x}_n + \boldsymbol{u}_n$. Accordingly, $\boldsymbol{x}_{ij} = \boldsymbol{x}_j - \boldsymbol{x}_i$ is the current axis vector of the stick i–j, that is, the relative position of the atom j with respect to the atom i. The vector $\boldsymbol{x}_{ij}$ can be expressed as

$$\boldsymbol{x}_{ij} = \mathbf{x}_{ij} + \boldsymbol{u}_{ij}, \tag{8}$$

where $\mathbf{x}_{ij} = \mathbf{x}_j - \mathbf{x}_i$, while $\boldsymbol{u}_{ij} = \boldsymbol{u}_j - \boldsymbol{u}_i$ (see Fig. 3).

Finally, the stick length and the unit vector of the stick i–j are given by, respectively,

$$r_{ij} = \sqrt{\boldsymbol{x}_{ij} \cdot \boldsymbol{x}_{ij}}, \tag{9a}$$

$$\boldsymbol{i}_{ij} = \boldsymbol{x}_{ij}/r_{ij}. \tag{9b}$$

The angle θ_{ijk} is defined in terms of the unit vectors $\boldsymbol{i}_{ij}$ and $\boldsymbol{i}_{ik}$ (see Fig. 4) to be

$$\cos\theta_{ijk} = \boldsymbol{i}_{ij} \cdot \boldsymbol{i}_{ik}. \tag{9c}$$

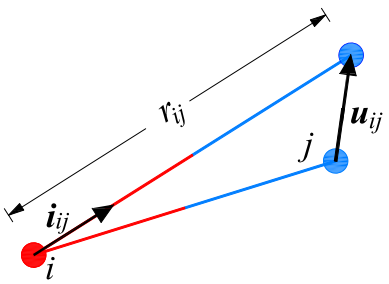

Fig. 3 Stick element

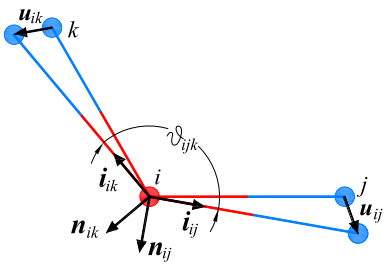

Fig. 4 Rotational spring element

We also need to introduce the directional derivatives of r_{ij} and θ_{ijk}. Recalling that $\frac{\partial \boldsymbol{x}_{ij}}{\partial \boldsymbol{u}_{ij}}\,\delta\boldsymbol{u}_{ij} = \delta\boldsymbol{u}_{ij}$, from Eqs. (9a) and (9b) we have

$$\delta r_{ij} = \left(\frac{\partial r_{ij}}{\partial \boldsymbol{u}_{ij}}\right)\cdot\delta\boldsymbol{u}_{ij} = \left(\frac{\partial r_{ij}}{\partial \boldsymbol{x}_{ij}}\right)\cdot\frac{\partial \boldsymbol{x}_{ij}}{\partial \boldsymbol{u}_{ij}}\,\delta\boldsymbol{u}_{ij} = \boldsymbol{i}_{ij}\cdot\delta\boldsymbol{u}_{ij}. \tag{10a}$$

By simple algebra, we also have that

$$\frac{\partial \boldsymbol{i}_{ij}}{\partial \boldsymbol{u}_{ij}}\delta\boldsymbol{u}_{ij} = \left(\frac{\mathrm{d}}{\mathrm{d}r_{ij}}\left(\frac{1}{r_{ij}}\right)\left(\frac{\partial r_{ij}}{\partial \boldsymbol{u}_{ij}}\right)\cdot\delta\boldsymbol{u}_{ij}\right)\boldsymbol{x}_{ij} + \frac{1}{r_{ij}}\frac{\partial \boldsymbol{x}_{ij}}{\partial \boldsymbol{u}_{ij}}\delta\boldsymbol{u}_{ij} = \frac{1}{r_{ij}}\left[\boldsymbol{I} - \boldsymbol{i}_{ij}\otimes\boldsymbol{i}_{ij}\right]\delta\boldsymbol{u}_{ij}. \tag{10b}$$

From Eq. (9c), it follows that

$$\delta\theta_{ijk} = \left(\frac{\partial\theta_{ijk}}{\partial \boldsymbol{u}_{ij}}\right)\cdot\delta\boldsymbol{u}_{ij} + \left(\frac{\partial\theta_{ijk}}{\partial \boldsymbol{u}_{ik}}\right)\cdot\delta\boldsymbol{u}_{ik}. \tag{11a}$$

For what follows, we identify the pair of sticks i–j and i–k through the indices $\alpha \in \{ij,\ ik\}$ and $\gamma \in \{ij,\ ik\}$, with $\gamma \neq \alpha$. We have

$$\left(\frac{\partial\theta_{ijk}}{\partial \boldsymbol{u}_{\alpha}}\right)\cdot\delta\boldsymbol{u}_{\alpha} = \frac{\mathrm{d}\theta_{ijk}}{d\cos\theta_{ijk}}\left(\frac{\partial\cos\theta_{ijk}}{\partial \boldsymbol{u}_{\alpha}}\right)\cdot\delta\boldsymbol{u}_{\alpha}, \tag{11b}$$

where

$$\frac{\mathrm{d}\theta_{ijk}}{d\cos\theta_{ijk}} = -\frac{1}{\sin\theta_{ijk}} \tag{11c}$$

and, due to Eq. (10b),

$$\left(\frac{\partial\cos\theta_{ijk}}{\partial \boldsymbol{u}_{\alpha}}\right)\cdot\delta\boldsymbol{u}_{\alpha} = \boldsymbol{i}_{\gamma}\cdot\left(\frac{\partial \boldsymbol{i}_{\alpha}}{\partial \boldsymbol{u}_{\alpha}}\delta\boldsymbol{u}_{\alpha}\right) = \frac{1}{r_{\alpha}}\left(\boldsymbol{i}_{\gamma} - \cos\theta_{ijk}\boldsymbol{i}_{\alpha}\right)\cdot\delta\boldsymbol{u}_{\alpha}. \tag{11d}$$

Substituting Eqs. (11b)–(11d) into Eq. (11a), we obtain that

$$\delta\theta_{ijk} = \frac{1}{r_{ij}}\,\boldsymbol{n}_{ij}\cdot\delta\boldsymbol{u}_{ij} + \frac{1}{r_{ik}}\,\boldsymbol{n}_{ik}\cdot\delta\boldsymbol{u}_{ik}, \tag{11e}$$

where

$$\boldsymbol{n}_{ij} = \frac{1}{\sin\theta_{ijk}}\left(\cos\theta_{ijk}\boldsymbol{i}_{ij} - \boldsymbol{i}_{ik}\right), \quad \boldsymbol{n}_{ik} = \frac{1}{\sin\theta_{ijk}}\left(\cos\theta_{ijk}\boldsymbol{i}_{ik} - \boldsymbol{i}_{ij}\right) \tag{11f}$$

are the unit vectors normal to the sticks in the plane that they define.

2.2.2 Equilibrium equations

The equilibrium configurations of the system are sought through the stationarity condition of its total potential energy

$$\Pi = U - \sum_{n}\boldsymbol{p}_{n}\cdot\boldsymbol{u}_{n}. \tag{12}$$

Recalling Eqs. (5), (10a) and (11e), the directional derivative of the potential U is

$$\begin{aligned}\delta U &= \sum_{b}\frac{\mathrm{d}U^{r}_{\mathrm{b}}}{\mathrm{d}r_{ij}}\delta r_{ij} + \sum_{a}\frac{\mathrm{d}U^{\theta}_{\mathrm{a}}}{\mathrm{d}\theta_{ijk}}\delta\theta_{ijk}\\ &= \sum_{b}\delta\boldsymbol{u}_{ij}\cdot\boldsymbol{f}_{ij} + \sum_{a}\left(\delta\boldsymbol{u}_{ij}\cdot\boldsymbol{t}_{ij} + \delta\boldsymbol{u}_{ik}\cdot\boldsymbol{t}_{ik}\right),\end{aligned} \tag{13a}$$

where

$$\boldsymbol{f}_{ij} = f_{ij}\boldsymbol{i}_{ij}, \quad \boldsymbol{t}_{ij} = \frac{m_{ijk}}{r_{ij}}\boldsymbol{n}_{ij}, \quad \boldsymbol{t}_{ik} = \frac{m_{ijk}}{r_{ik}}\boldsymbol{n}_{ik} \tag{13b}$$

are the force vectors of the elements (see Figs. 5 and 6).

Then, expressing the vectors $\delta\boldsymbol{u}_{ij}$ and $\delta\boldsymbol{u}_{ik}$ of the sticks in terms of nodal quantities, the equilibrium equations are given by

$$\sum_b \boldsymbol{f}_{ij} \cdot (\delta\boldsymbol{u}_j - \delta\boldsymbol{u}_i) + \sum_a \left[\boldsymbol{t}_{ij} \cdot (\delta\boldsymbol{u}_j - \delta\boldsymbol{u}_i) + \boldsymbol{t}_{ik} \cdot (\delta\boldsymbol{u}_k - \delta\boldsymbol{u}_i)\right] = \sum_n \boldsymbol{p}_n \cdot \delta\boldsymbol{u}_n \tag{13c}$$

for any $\delta\boldsymbol{u}_n$.

2.2.3 Linearization of the stick-and-spring model

In the previous subsections, the stick-and-spring model has been introduced in its general nonlinear form. Here, it is linearized about a given reference configuration, which we will denote using " ˜ ".

So, Eq. (4) can be rewritten as

$$U_{\mathrm{b}}^r = \tilde{U}_{\mathrm{b}}^r + \tilde{f}_{ij}\Delta r_{ij} + \frac{1}{2}\tilde{k}_{ij}\Delta r_{ij}^2, \tag{14a}$$

$$U_a^\theta = \tilde{U}_{\mathrm{a}}^\theta + \tilde{m}_{ijk}\Delta\theta_{ijk} + \frac{1}{2}\tilde{k}_{ijk}\Delta\theta_{ijk}^2, \tag{14b}$$

where $\Delta r_{ij} = r_{ij} - \tilde{r}_{ij}$ and $\Delta\theta_{ijk} = \theta_{ijk} - \tilde{\theta}_{ijk}$.

Accordingly, Eq. (5) becomes

$$f_{ij} = \tilde{f}_{ij} + \tilde{k}_{ij}\Delta r_{ij}, \tag{15a}$$

$$m_{ijk} = \tilde{m}_{ijk} + \tilde{k}_{ijk}\Delta\theta_{ijk}, \tag{15b}$$

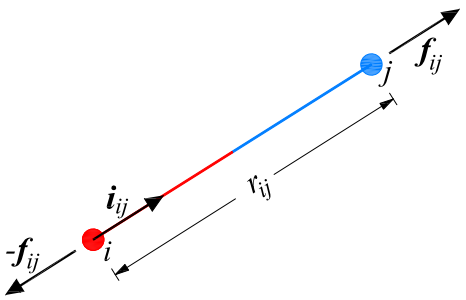

Fig. 5 Stick element response

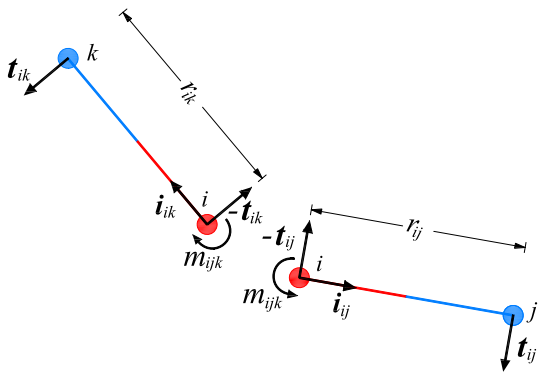

Fig. 6 Rotational spring element response

while the rigidities are

$$k_{ij} = \tilde{k}_{ij}, \tag{16a}$$

$$k_{ijk} = \tilde{k}_{ijk}. \tag{16b}$$

Making use of Eqs. (10a) and (11e), we have

$$\Delta r_{ij} = \tilde{\boldsymbol{\imath}}_{ij} \cdot \boldsymbol{u}_{ij}, \tag{17a}$$

$$\Delta\theta_{ijk} = \frac{1}{\tilde{r}_{ij}} \tilde{\boldsymbol{n}}_{ij} \cdot \boldsymbol{u}_{ij} + \frac{1}{\tilde{r}_{ik}} \tilde{\boldsymbol{n}}_{ik} \cdot \boldsymbol{u}_{ik}. \tag{17b}$$

Finally, the equilibrium is given by Eq. (13c), in which the force vectors of the elements are $\boldsymbol{f}_{ij} = f_{ij}\tilde{\boldsymbol{\imath}}_{ij}$, $\boldsymbol{t}_{ij} = \frac{m_{ijk}}{\tilde{r}_{ij}} \tilde{\boldsymbol{n}}_{ij}$ and $\boldsymbol{t}_{ik} = \frac{m_{ijk}}{\tilde{r}_{ik}} \tilde{\boldsymbol{n}}_{ik}$, with f_{ij} and m_{ijk} given by Eqs. (15) and (17).

3 Preliminaries to the simulations

The nonlinear stick-and-spring model and its linearization are, respectively, used to study the relaxed configurations and the elastic constants of several CNTs, BNNTs and SiCNTs. In all cases, nanotubes of both armchair and zigzag type are considered, by varying the indices $n = m \in \{3, 4, 5, 8, 12, 16\}$ and $n \in \{5, 7, 9, 14, 20, 26\}$, respectively.

One objective of this work is to test the model with the force constants and the well depth values given in the literature [41,67,74,95,99] and listed in Table 1, where we also report the adopted resting bond lengths, taken from [36].

Comparisons with available ab-initio results are given and, when necessary, used to refine the values of the force constants.

In order to make comparisons with the existing literature, we must obtain solutions that are as periodic as possible, by minimizing the disturbances due to constraints or bond truncations at the end sections. For this purpose, we select high aspect ratios ℓ/ϱ of about 40 and, in addition, we use constraint conditions which do not introduce any local disturbances to the cross-sectional deformation (e.g. necking effects or transversal dilatations of the cross sections). In particular, we filter the rigid body motion of the tube through the following constraint equations:

$$\sum_i \boldsymbol{u}_i = \boldsymbol{0}, \quad \sum_i \boldsymbol{u}_i \times \mathbf{x}_i = \boldsymbol{0}, \tag{18}$$

where the summation extends over the line of atoms at $z = 0$ for armchair nanotubes and over the two lines of atoms closest to $z = 0$ for zigzag nanotubes.

The constraint conditions of Eq. (18) are added through Lagrange multipliers. The equations of the problem are numerically solved using the Newton–Raphson method and the expression of the iteration matrix can be found in the Appendix. In the linear contexts, the iteration matrix is assembled and decomposed only at the initial step and the iteration scheme is used only to correct rounding errors without significant extra costs.

For the computations, custom-made `MATLAB` computer code has been implemented. The output results are displayed using the `Gmsh` [98] post-processor.

Table 1 Constitutive parameters for the selected tubes

	Atom type		Parameter values				
	1	2	r_e (nm)	D (nN nm)	k_r (nN/nm)	$\mathcal{K}_1$ (nN nm/rad^2)	$\mathcal{K}_2$ (nN nm/rad^2)
C	C	C	0.142	0.79	742	1.42	1.42
BN	B	N	0.145	0.64	585	1.347	0.641
SiC	Si	C	0.177	0.74	405	0.648	0.957

4 The tubes relaxed configuration

In this section, we evaluate the relaxed configuration of the tubes, by solving Eq. (13c) for zero loads $\boldsymbol{p}_n$ and under the constraint conditions given in Eq. (18). Case by case, we quantify the distance between the ideal and relaxed configurations. Furthermore, we give comparisons with the ab-initio results. By so doing, we emphasize also the implications of having two angular force constants for a diatomic tube and we refine their values for SiC hexagonal nanomaterials.

4.1 CNTs

Our numerical simulations show nearly cylindrical configurations, essentially characterized by greater radii and smaller lengths than the ideal ones. In Table 2, the ideal radii and lengths are compared to mean radii and lengths in the relaxed configurations. The listed measures highlight that the distances between the two configurations are extremely small and tend to fade away as the radius increases. At most, we find differences of about 4.6% for the radius and of about 3.4% for the length, for the smallest nanotube, the one given by (5,0).

For further insight, Fig. 7 shows the relaxed configurations of the (5,0) and the (3,3) CNTs. The chromatic maps provide the radius value corresponding to each atom row. In the top and bottom boxes, the regions of the nanotubes near the bases are shown in greater detail. The related measures of the radius and of the distance between the atom rows along the tube axis are reported until no more end effects can be seen. The detail in the middle of the figure shows a section of the (3,3) CNT, found within the undisturbed region. The central angles are reported. Any value in round brackets refers to the ideal configuration.

Analysing the figure, first we notice that in both cases the end effects are really negligible, since they involve only very few atom rows near the bases. Moreover, if we focus our attention on the local effects, we note that for the zigzag case the axial shortening does not involve the sticks parallel to the tube axis, while, for the armchair case, variations in the central angles are registered. These trends are similar to what has been observed in [78] for CNTs under radial loads.

At this point, to provide the numerical assessment of the adopted model, we compare some radii from Table 2 with the corresponding values found in the literature, obtained through ab-initio simulations. This comparison is summarized in Table 3. Our numerical results are in excellent agreement with the ab-initio values, in the sense that we see differences between them and our numerics which are of the same order as the differences found between the various ab-initio values reported in the literature. The maximum percentage difference, of about 6.0%, is registered in the case of the (14,0) tube, for which the literature provides only one result [40].

Table 2 Radii and lengths of CNTs in ideal and relaxed configurations

CNTs	Ideal conf.		Relaxed conf.	
	ϱ (Å)	ℓ (Å)	ϱ (Å)	ℓ (Å)
(3,3)	2.034	83.62	2.093	82.45
(4,4)	2.712	108.22	2.756	107.33
(5,5)	3.390	137.73	3.427	136.99
(8,8)	5.424	221.36	5.447	220.89
(12,12)	8.136	332.03	8.151	331.72
(16,16)	10.848	437.79	10.860	437.56
(5,0)	1.957	79.52	2.051	76.87
(7,0)	2.740	109.34	2.808	107.47
(9,0)	3.523	143.42	3.576	141.94
(14,0)	5.480	220.10	5.515	219.17
(20,0)	7.829	318.08	7.853	317.42
(26,0)	10.178	411.80	10.196	411.30

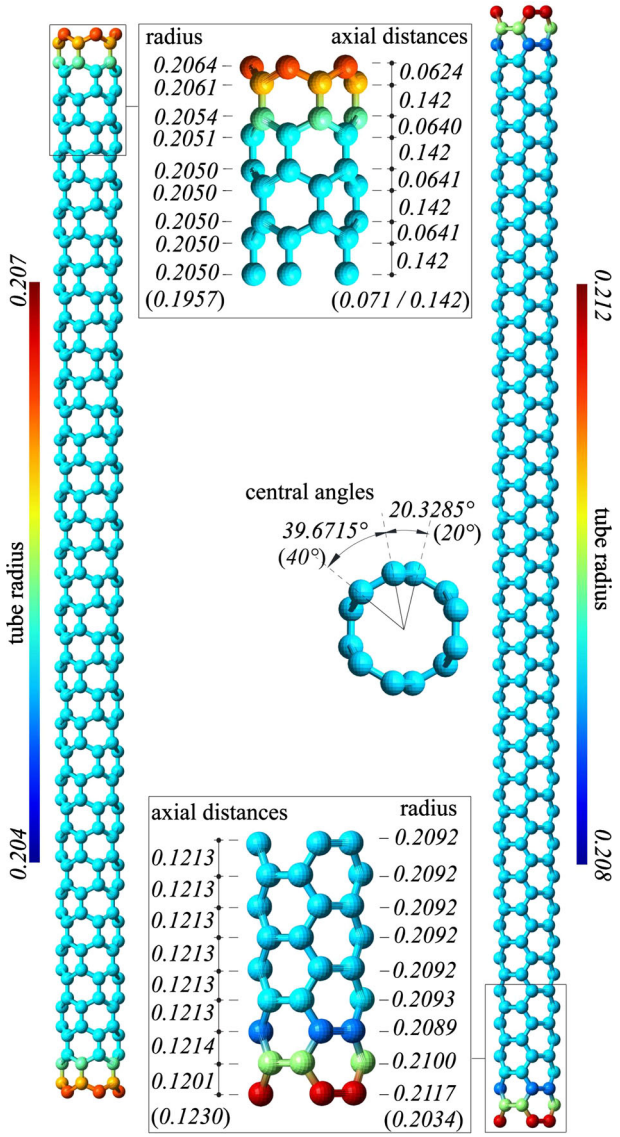

Fig. 7 Relaxed configurations of the (5,0) and the (3,3) CNTs

4.2 BNNTs

The relaxed configuration of BNNTs is quite different from that of CNTs. We find that it assumes a radially buckled shape, in agreement with the ab-initio results [27,32,34]. Figure 8 shows the relaxed configurations provided by our simulations for the (5,0) and the (3,3) BNNTs. B and N atoms are represented by spheres of dimension proportional to the atomic radius, the atomic radius of N being smaller than that of B. The relaxed configurations are essentially characterized by two concentric cylindrical surfaces of mean radius ϱ_1 and ϱ_2, on which B and N atoms place themselves. Overall, the mean value of the two radii is greater than the ideal one and the tube undergoes a shortening (see Table 4).

By analysing Fig. 8, we observe that the buckled shape depends on the chirality, developing along the axial direction for the zigzag tubes and along the circumferential direction for the armchair tubes. In the middle of the figure, some details are given which provide interesting insights. Similarly to the CNTs, in the zigzag case, the shortening of the tube induced by relaxation practically involves only the portions related to the initially oblique sticks and, in the armchair case, variations in the central angles are also registered.

Table 3 Radius values in (Å) of some CNTs in the relaxed configuration compared with the literature

CNTs	(3,3)	(4,4)	(5,5)	(8,8)	(12,12)	(5,0)	(7,0)	(9,0)	(14,0)	(20,0)
Ideal radius	2.034	2.712	3.390	5.424	8.136	1.957	2.740	3.523	5.480	7.829
Present work	2.093	2.756	3.427	5.447	8.151	2.051	2.808	3.576	5.155	7.853
[26]	–	2.794	3.463	5.498	–	–	–	–	–	–
[27]	–	2.786	–	–	–	–	2.816	–	–	–
[28]	2.100	–	–	–	–	2.035	–	–	–	–
[29]	2.120	–	–	–	–	2.060	–	–	–	–
[30]	2.120	2.750	–	–	–	2.050	–	–	–	–
[37]	2.111	2.775	3.445	5.472	–	–	–	–	–	–
[38]	–	–	3.434	–	–	2.041	–	–	–	–
[39]	2.100	2.765	3.430	–	–	2.035	2.795	–	–	–
[40]	–	–	3.395	5.435	8.150	–	2.745	3.535	5.485	7.835

If we analyse in more detail the measures shown in Table 4, we see that the differences between ideal and relaxed quantities are extremely small and they tend to vanish as the radius increases. At most, we find differences of about 5% for the radius ϱ_2 and of about 3.3% for the tube length, for the smallest nanotube, that is (5,0).

In Table 5, we provide a comparison between the quantities obtained from our simulations with those provided by ab-initio results in the literature. Our numerical results are in excellent agreement with the ab-initio values, as before. The maximum percentage difference, of about 5.0%, is registered for the (5,0) nanotube, where ϱ_1 is about 5.0% smaller with respect to the value reported in [34].

Although it might seem obvious, it is worth highlighting that the appearance of the buckled configuration is due to the diversification of the angular force constant for the two atom types, as in the UFF potential [96], but not the DREIDING one. In this regard, the available parametrizations of the Tersoff–Brenner potential [43,49,95] need improvements, because they don't diversify the angular parameters. That said, our results show that the atoms related to the force constant with the lower value are positioned on the larger cylinder, and vice versa. At the same time, all the ab-initio results [27,32–35] referring to the diatomic nanotubes agree that the placement of the atoms is related to higher or lower electronegativity,[2] with the most electronegative ones sitting on the larger cylinder. Therefore, the force constant with lower value has to correspond to the more electronegative atoms. Our results concerning BNNTs are consistent with this theoretical framework, since the force constant with lower value corresponds to the more electronegative N atoms, and, vice versa, the force constant with the higher value corresponds to the less electronegative B atoms.

4.3 SiCNTs

In the case of SiCNTs, the ab-initio results [33–35] show that Si and C atoms lie on the cylinder with smaller and greater radius, respectively, in accordance with the electronegativity rule. However, the values in Table 1 for SiCNTs are not in agreement with this trend, because the smaller value of the angular force constant is attributed to the less electronegative Si atom.

In [74], we evaluated the force constants listed in Table 1, based upon certain assumptions. The first two assumptions were the analytical expressions of the surface Young's modulus E and Poisson ratio ν of a diatomic sheet

$$E = \frac{4\sqrt{3}k_r\,(\mathcal{K}_1 + \mathcal{K}_2)}{k_r r_e^2 + 9\,(\mathcal{K}_1 + \mathcal{K}_2)}, \tag{19a}$$

$$\nu = \frac{k_r r_e^2 - 3(\mathcal{K}_1 + \mathcal{K}_2)}{k_r r_e^2 + 9(\mathcal{K}_1 + \mathcal{K}_2)}, \tag{19b}$$

where the quantities k_r and $(\mathcal{K}_1 + \mathcal{K}_2)$ were calculated from ab-initio estimates of E and ν.[3] Then, to obtain the individual values of $\mathcal{K}_1$ and $\mathcal{K}_2$, we added a third equation, suggested in [96], which states that the ratio

[2] The electronegativity is the measure of an atom's ability to attract electrons to itself when bonding with another atom. Excluding the noble gases, the electronegativity values tend to increase going towards the top right of the periodic table.

[3] In [74], the ab-initio reference values have been taken from [36].

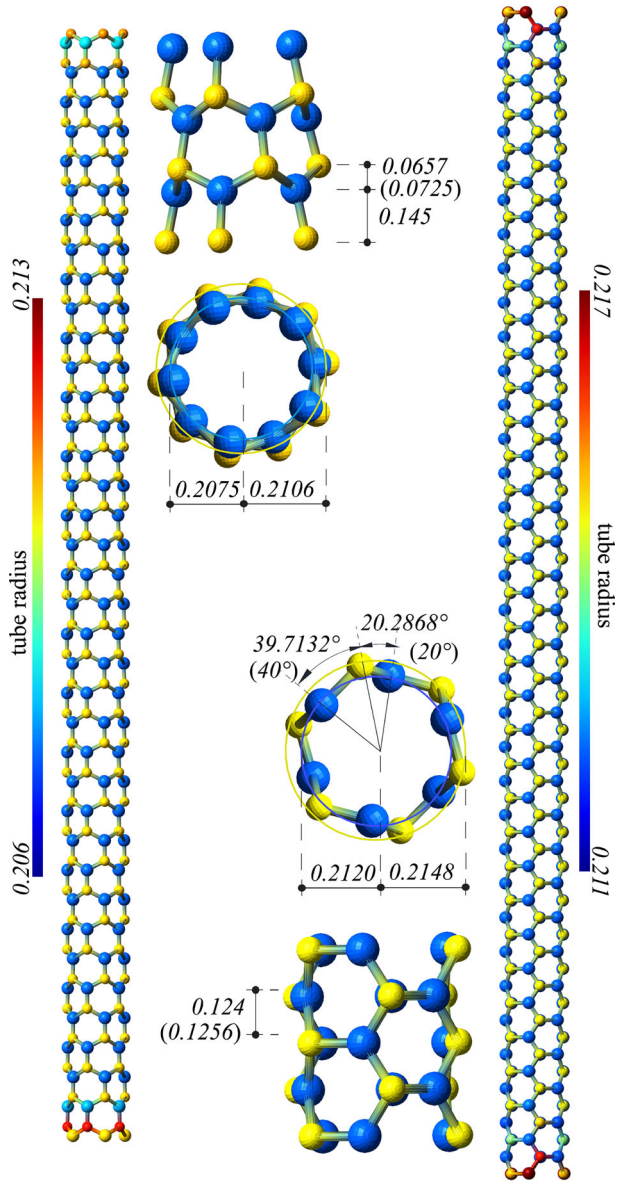

Fig. 8 Relaxed configurations of the (5,0) and the (3,3) BNNTs

Table 4 Radii and lengths of BNNTs in ideal and relaxed configurations

BNNTs	Ideal conf.		Relaxed conf.		
	ϱ (Å)	ℓ (Å)	ϱ_1 (Å)	ϱ_2 (Å)	ℓ (Å)
(3,3)	2.077	85.39	2.121	2.149	84.27
(4,4)	2.769	110.50	2.804	2.823	109.65
(5,5)	3.462	140.64	3.490	3.505	139.93
(8,8)	5.539	226.03	5.557	5.566	225.58
(12,12)	8.308	339.05	8.320	8.326	338.75
(16,16)	11.077	447.04	11.086	11.091	446.82
(5,0)	1.999	81.20	2.076	2.107	78.58
(7,0)	2.798	111.65	2.856	2.876	109.80
(9,0)	3.597	146.45	3.643	3.658	144.99
(14,0)	5.596	224.75	5.626	5.635	223.83
(20,0)	7.994	324.80	8.015	8.021	324.15
(26,0)	10.393	420.50	10.409	10.413	420.00

Table 5 Radius in (Å) of some BNNTs in the relaxed configuration compared with ab-initio results the literature

Tube	Ideal	Present		Kudin [27]		Jia [32]		Baumeier [34]	
	ϱ	ϱ_1	ϱ_2	ϱ_1	ϱ_2	ϱ_1	ϱ_2	ϱ_1	ϱ_2
(3,3)	2.077	2.121	2.149	–	–	2.044	2.159	–	–
(4,4)	2.769	2.804	2.823	2.816	2.865	2.736	2.819	2.701	2.790
(5,5)	3.462	3.490	3.505	–	–	3.426	3.488	3.401	3.469
(8,8)	5.539	5.557	5.566	–	–	5.485	5.523	5.455	5.495
(5,0)	1.999	2.076	2.107	–	–	2.000	2.113	1.979	2.101
(7,0)	2.798	2.856	2.876	2.863	2.921	2.786	2.862	2.758	2.843
(9,0)	3.593	3.643	3.658	–	–	3.572	3.629	3.543	3.607
(14,0)	5.596	5.628	5.635	–	–	5.553	5.588	–	–

Table 6 Reference ab-initio radii in (Å) of SiCNTs in the literature

Tube	Zhao [33]		Baumeier [34]		Alam [35]	
	ϱ_1	ϱ_2	ϱ_1	ϱ_2	ϱ_1	ϱ_2
(3,3)	–	–	–	–	2.638	2.675
(4,4)	–	–	3.295	3.436	3.495	3.528
(5,5)	4.272	4.368	4.136	4.245	4.366	4.394
(8,8)	–	–	6.668	6.733	6.945	6.961
(5,0)	–	–	2.401	2.590	–	–
(7,0)	–	–	3.358	3.492	–	–
(9,0)	–	–	4.324	4.426	–	–

$\mathcal{K}_1/\mathcal{K}_2$ is proportional to the ratio of the square effective charge of the atom type 2 over the square effective charge of the atom type 1. However, this assumption no longer seems to be convincing in the light of the above considerations on the relaxed configuration of SiCNTs, even if, in the case of BNNTs, it has provided results in agreement with the electronegativity rule.

Therefore, for SiCNTs we need a new third condition to add to Eq. (19). We propose to minimize the distance between the radial buckling parameter $(\varrho_1 - \varrho_2)$ provided by our simulations for several SiCNTs and the same parameter $(\varrho_1^* - \varrho_2^*)$ obtained through ab-initio methods for the same SiCNTs and listed in Table 6.

Specifically, for a discrete number of values of $\mathcal{K}_1$ ranging from $(\mathcal{K}_1 + \mathcal{K}_2)/2$ to $(\mathcal{K}_1 + \mathcal{K}_2)$, ϱ_1 and ϱ_2 are obtained numerically for any tube given in Table 6. The selected value of $\mathcal{K}_1$ is the one that minimizes the function

$$\sum_t \left(\frac{\varrho_1 - \varrho_2}{\varrho_1^* - \varrho_2^*} - 1 \right)^2, \tag{20}$$

where the summation extends over all the tubes.

In this case, the minimum condition provides the values $\mathcal{K}_1 = 1.264$ nNnm/rad^2 and $\mathcal{K}_2 = 0.341$ nNnm/rad^2.

With the new force constants, the relaxed configuration for any SiCNT has been evaluated and compared to the ideal configuration in Table 7. For the (5,0) nanotube, differences of about 5.5% for the radius ϱ_2 and of about 3.2% for the length are found.

Table 8 compares some radii from Table 7 with the available ab-initio values from Table 6. A general agreement between the radii obtained by this minimization and the values from the literature is found. In particular, for the (5,0) nanotube the obtained radius ϱ_1 differs by less than 5.0% with respect to the value reported in [34].

5 The elastic constants

Uniform tensile, radial and torsional tests are now performed, by considering three-point force systems (see Fig. 9) consisting of: axial forces F_z applied to the atoms of the tube free end sections (tensile tests); circumferential forces F_θ applied to the atoms of the tube free end sections (torsional tests); and radial forces P_i applied to each atom i of the tube (radial tests).

Table 7 Radii and lenghts of SiCNTs in ideal and relaxed configurations

SiCNTs	Ideal conf.		Relaxed conf.		
	ϱ (Å)	ℓ (Å)	ϱ_1 (Å)	ϱ_2 (Å)	ℓ (Å)
(3,3)	2.535	104.23	2.571	2.630	103.04
(4,4)	3.380	134.89	3.410	3.452	133.97
(5,5)	4.226	171.68	4.250	4.282	170.92
(8,8)	6.761	275.92	6.777	6.796	275.43
(12,12)	10.141	413.87	10.152	10.165	413.55
(16,16)	13.522	545.70	13.530	13.540	545.56
(5,0)	2.440	99.12	2.513	2.581	96.10
(7,0)	3.415	136.29	3.472	3.515	134.16
(9,0)	4.391	178.77	4.437	4.469	177.08
(14,0)	6.831	274.35	6.861	6.881	273.28
(20,0)	9.759	396.48	9.780	9.793	395.73
(26,0)	12.686	513.30	12.702	12.713	512.72

Table 8 Radius in (Å) of some SiCNTs in the relaxed configuration compared with ab-initio results from the literature

Tube	Ideal	Present		Zhao [33]		Baumeier [34]		Alam [35]	
	ϱ	ϱ_1	ϱ_2	ϱ_1	ϱ_2	ϱ_1	ϱ_2	ϱ_1	ϱ_2
(3,3)	2.535	2.571	2.630	–	–	–	–	2.638	2.675
(4,4)	3.380	3.410	3.452	–	–	3.295	3.436	3.495	3.528
(5,5)	4.226	4.250	4.282	4.272	4.368	4.136	4.245	4.366	4.394
(8,8)	6.761	6.777	6.796	–	–	6.668	6.733	6.945	6.961
(5,0)	2.440	2.513	2.581	–	–	2.401	2.590	–	–
(7,0)	3.415	3.472	3.515	–	–	3.358	3.492	–	–
(9,0)	4.391	4.437	4.469	–	–	4.324	4.426	–	–

The elastic constants are calculated by referring to the membrane states of an homogeneous orthotropic Donnell thin shell [97]. Comparisons with the available ab-initio results are given.

The negligible differences in terms of length and of radius between the ideal and the relaxed configurations make it plausible to consider a continuum model equivalent to the nanotube in the ideal configuration, an assumption that is frequently found in the literature (e.g. [41,49,51,54,64,78,82,83]). With this in mind, the tests are performed using the linearized version of the stick-and-spring model about the ideal configuration. In addition, Eq. (15) are simplified, by assuming $\tilde{f}_{ij} = \tilde{m}_{ijk} = 0$ and substituting the rigidities $\tilde{k}_{ij}$ and $\tilde{k}_{ijk}$ for those in the planar configuration, because the differences are negligible. Accordingly, $\tilde{k}_{ij} = k_r$ and $\tilde{k}_{ijk} = k_\theta$ are used.

For the reader's convenience, we recall the equations governing the equilibrium problem of the membrane behaviour of the cylindrical shell, under the hypotheses of uniform stress/strain and hyperelasticity. They are

$$N_z = \text{const.}, \quad N_\theta = p\varrho, \quad N_{z\theta} = \text{const.}, \tag{21a}$$

$$\varepsilon_z = \frac{\partial u}{\partial z} = \text{const.}, \quad \varepsilon_\theta = \frac{w}{\varrho} = \text{const.}, \quad \gamma_{z\theta} = \frac{\partial v}{\partial z} = \text{const.}, \tag{21b}$$

$$N_z = \frac{E_z}{\Delta}\varepsilon_z + \frac{\nu_{\theta z}E_z}{\Delta}\varepsilon_\theta, \quad N_\theta = \frac{\nu_{z\theta}E_\theta}{\Delta}\varepsilon_z + \frac{E_\theta}{\Delta}\varepsilon_\theta, \quad N_{z\theta} = G\gamma_{z\theta}, \tag{21c}$$

$$E_z/E_\theta = \nu_{z\theta}/\nu_{\theta z}. \tag{21d}$$

In Eq. (21), u, v and w are the axial, circumferential and radial displacements (see Fig. 10), ε_z, ε_θ and $\gamma_{z\theta}$ are the axial, circumferential and shearing strains, N_z, N_θ and $N_{z\theta}$ are the related inner forces, while p is the uniform pressure. Finally, E_z, E_θ and G are the surface Young's modulus and the shear moduli, $\nu_{z\theta}$ and $\nu_{\theta z}$ the Poisson ratios and $\Delta = 1 - \nu_{z\theta}\nu_{\theta z}$.

For what follows, we need to specify the component-wise displacements of the ith atom, which we denote by u_i, v_i and w_i. To link the continuum and the stick-and-spring models, we assume a proper correspondence

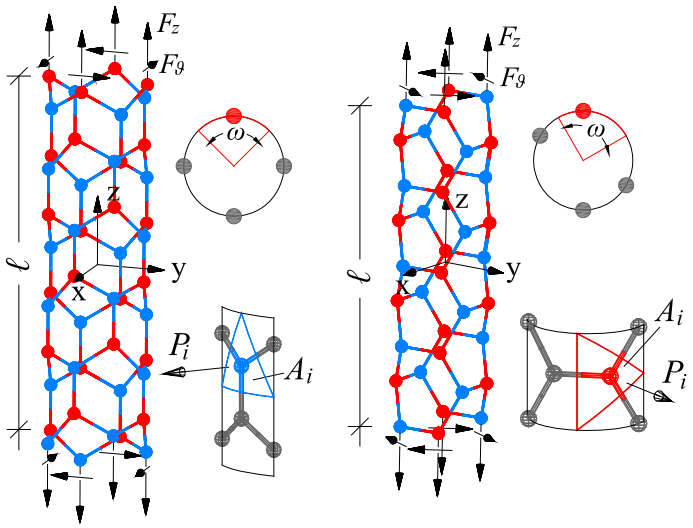

Fig. 9 Applied loads

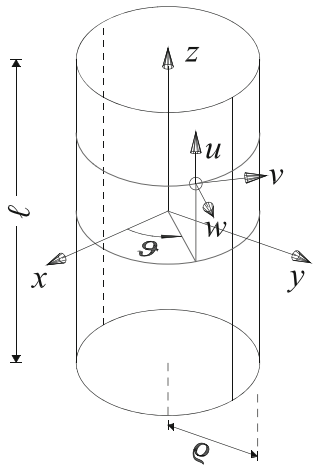

Fig. 10 Displacements of the Donnell shell

in terms of their displacements. In particular, we assume that the axial and circumferential displacements of the shell end bases (at $z = \pm\ell/2$) are given by

$$u[\pm\ell/2] = \frac{1}{n_s}\sum_i u_i, \quad v[\pm\ell/2] = \frac{1}{n_s}\sum_i v_i, \tag{22a}$$

where n_s is the atom number of the tube section and the summations extend over the section at hand. In addition, we assume that the radial displacement of the shell is

$$w = \frac{1}{2\pi\varrho\ell}\sum_i w_i \mathcal{A}_i, \tag{22b}$$

where $\mathcal{A}_i$ is the reference area of the ith atom, while the summation extends over the entire tube.

Now, we can relate the external forces F_z, F_θ and P_i to the shell stresses N_z, $N_{z\theta}$ and N_θ through work equivalences. In particular, F_z and F_θ are related to N_z and $N_{z\theta}$ by equating the work of the tractions applied to the base at $z = \ell/2$ to its discrete counterpart

$$2\pi\varrho N_z u[\ell/2] = F_z\sum_i u_i, \quad 2\pi\varrho N_{z\theta} v[\ell/2] = F_\theta\sum_i v_i. \tag{23a}$$

Now, recalling Eqs. (22a) and (23a) provides

$$F_z = N_z \omega \varrho, \quad F_\theta = N_{z\theta} \omega \varrho, \tag{23b}$$

where $\omega = \dfrac{2\pi}{n_s}$ is the central angle related to each atom (see Fig. 9). Similarly, the forces P_i are related to N_θ through the equality

$$2\pi \varrho \ell w p = \sum_i P_i w_i, \tag{23c}$$

which involves the work of the pressure p and its discrete counterpart. Recalling Eqs. (21a) and (22b) and imposing that Eq. (23c) be satisfied for each w_i, we obtain

$$P_i = \frac{N_\theta}{\varrho} \mathcal{A}_i. \tag{23d}$$

5.1 Numerical results and discussion

The numerical analyses are performed using the constraints of Eq. (18) and evaluating the forces F_z, F_θ and P_i from Eqs. (23b) and (23d), by setting the values of N_z, N_θ, $N_{z\theta}$ in the following three ways:

1. $N_z = 1$ nN/nm, $N_\theta = N_{z\theta} = 0$;
2. $N_\theta = 1$ nN/nm, $N_z = N_{z\theta} = 0$;
3. $N_{z\theta} = 1$ nN/nm, $N_z = N_\theta = 0$.

The elastic constants are then obtained by evaluating the strains using Eq. (21b) and the map given in Eq. (22). For further details see [78].

Tables 9, 10 and 11 show the values of the elastic constants of the membrane behaviour obtained for the three types of tubes and the range of their mean values, that is, the arithmetic mean between the values relative to minimum and maximum radii.

The results show a moderate dependence of the elastic constants on the tube radius and chirality. For all cases, the surface Young's moduli E_z and E_θ and the shear modulus G increase, whereas the Poisson ratios $\nu_{z\theta}$ and $\nu_{\theta z}$ decrease, as the radius increases. The radius does not have the same influence on all the constants. The shear modulus G of the armchair tubes is shown to be the most sensitive one, with differences of about 18.0% with respect to the range mean value in the case of SiCNTs, whereas in the other cases the differences are slightly smaller. Overall, the results show a clear consistency with Eq. (21d), with both the ratios between E_z and E_θ and between $\nu_{z\theta}$ and $\nu_{\theta z}$ almost equal to 1. Especially for the smallest radii, the value of G, obtained by the torsion test, is significantly different from the value obtainable from the tensile test under the isotropy hypothesis, with maximum difference of more than 30.0% for (3,3) CNT and (3,3) BNNT. Therefore, the nanotubes are not isotropic. Finally, it is worth noting that the CNTs are stiffer than the other tubes, with range mean values of the surface Young's modulus and shear moduli of about 1.4 times those of BNNTs and of about 2.3 times those of SiCNTs and with range mean values of the Poisson ratios of about 0.7 and 0.5 times those of BNNTs and of SiCNTs, respectively.

Tables 12, 13 and 14 show the comparison between our results and the ab-initio results in the literature, concerning the surface Young's modulus E_z. As opposed to what has been observed for the relaxed radii, not all the ab-initio results are in agreement amongst themselves. In this respect, a relevant discrepancy between the values provided in [40] with respect to the other ones arises and it is difficult for us to express any judgement about it. However, our results are in reasonable agreement with all the other references, with the maximum difference of about 10.0% with respect to [38] for the (5,0) CNT and of about 6.0% and 6.6% with respect to [34] for the (8,8) BNNT and for the (8,8) SiCNT, respectively.

Overall, this good correspondence can be considered as a further verification of the selected force constants and of the assumptions employed for evaluating the elastic constants of the tubes. Of course, some aspects have been deliberately ignored, such as the radial buckling of the relaxed diatomic tubes and the presence of a self-stress state in some elements, but this has not produced significant errors even in the case of the smallest radii, characterized by greater variations in the bond lengths and angles with respect to the sheets. However, these aspects might be significant in nonlinear contexts, such as in imperfection sensitivity analysis or in strength evaluation under tensile loads.

Table 9 Elastic constants of CNTs

CNTs	E_z (N/m)	E_θ (N/m)	$\nu_{z\theta}$	$\nu_{\theta z}$	G (N/m)
(3,3)	344.2	342.6	0.1908	0.1900	107.6
(4,4)	350.5	350.6	0.1783	0.1784	126.7
(5,5)	353.7	354.4	0.1719	0.1722	136.5
(8,8)	357.4	358.4	0.1644	0.1649	147.8
(12,12)	358.8	359.8	0.1616	0.1620	152.0
(16,16)	359.4	360.2	0.1605	0.1609	153.5
Range mean value	351.8 ± 7.6	351.4 ± 8.8	0.1756 ± 0.015	0.1754 ± 0.014	130.5 ± 22.9
(5,0)	331.7	324.0	0.2276	0.2224	140.0
(7,0)	343.9	341.1	0.1969	0.1953	147.6
(9,0)	349.8	348.7	0.1828	0.1823	150.8
(14,0)	355.5	355.8	0.1693	0.1695	153.6
(20,0)	357.7	358.3	0.1644	0.1645	154.6
(26,0)	358.7	359.2	0.1622	0.1624	155.0
Range mean value	345.2 ± 13.5	341.6 ± 17.6	0.1949 ± 0.0327	0.1924 ± 0.03	147.5 ± 7.5

Table 10 Elastic constants of BNNTs

BNNTs	E_z (N/m)	E_θ (N/m)	$\nu_{z\theta}$	$\nu_{\theta z}$	G (N/m)
(3,3)	249.6	249.6	0.2529	0.2529	75.85
(4,4)	254.4	255.2	0.2416	0.2424	89.54
(5,5)	256.9	257.8	0.2357	0.2366	96.56
(8,8)	259.8	260.8	0.2288	0.2297	104.7
(12,12)	260.9	261.7	0.2262	0.2269	107.8
(16,16)	261.4	262.1	0.2252	0.2258	108.9
Range mean value	255.5 ± 5.9	255.8 ± 6.2	0.2390 ± 0.014	0.2393 ± 0.013	92.37 ± 16.5
(5,0)	240.1	237.2	0.2884	0.2849	99.49
(7,0)	249.4	249.4	0.2594	0.2594	104.8
(9,0)	253.9	254.7	0.2461	0.2469	107.0
(14,0)	258.3	259.6	0.2333	0.2344	109.0
(20,0)	260.1	261.2	0.2284	0.2295	109.7
(26,0)	260.9	261.9	0.2265	0.2274	110.0
Range mean value	250.4 ± 10.3	248.0 ± 13.3	0.259 ± 0.032	0.256 ± 0.028	104.7 ± 5.2

Table 11 Elastic constants of SiCNTs

SiCNTs	E_z (N/m)	E_θ (N/m)	$\nu_{z\theta}$	$\nu_{\theta z}$	G (N/m)
(3,3)	148.5	149.8	0.3519	0.3551	43.77
(4,4)	151.5	152.9	0.3434	0.3464	51.86
(5,5)	153.2	154.3	0.3388	0.3414	56.04
(8,8)	155.1	156.0	0.3333	0.3355	60.92
(12,12)	155.9	156.5	0.3312	0.3325	62.77
(16,16)	156.2	156.7	0.3304	0.3314	63.43
Range mean value	152.3 ± 3.8	153.2 ± 3.4	0.3411 ± 0.011	0.3432 ± 0.012	53.6 ± 9.8
(5,0)	142.7	141.5	0.3861	0.3828	58.13
(7,0)	148.5	148.9	0.3603	0.3614	61.19
(9,0)	151.3	152.2	0.3485	0.3505	62.46
(14,0)	154.2	155.2	0.3372	0.3394	63.60
(20,0)	155.4	156.2	0.3330	0.3349	64.00
(26,0)	155.9	156.6	0.3313	0.3329	64.15
Range mean value	149.3 ± 6.6	148.1 ± 8.1	0.3604 ± 0.029	0.3572 ± 0.024	61.1 ± 3.0

Table 12 E_z (N/m) of CNTs compared with the literature

CNTs	E_z	[27]	[31]	[37]	[38]	[39]	[40]
(3,3)	344.2	–	331.0	322.0	–	319.0	–
(4,4)	350.5	333.0	344.0	341.0	–	323.0	–
(5,5)	353.7	–	348.0	346.0	331.64	329.0	439.62
(8,8)	357.4	–	–	354.0	–	–	440.64
(12,12)	358.8	–	–	–	–	–	454.58
(5,0)	331.7	–	321.0	–	303.51	305.0	
(7,0)	343.9	333.0	–	–	–	334.0	
(9,0)	349.8	–	–	–	–	–	430.78
(14,0)	355.5	–	–	–	–	–	455.26
(20,0)	357.7	–	–	–	–	–	460.02

Table 13 E_z (N/m) of BNNTs compared with the literature

BNNTs	E_z	[27]	[34]	[40]
(4,4)	254.4	258.0	268.0	–
(5,5)	256.9	–	272.0	–
(8,8)	259.8	–	276.0	–
(5,0)	240.1	–	246.0	–
(7,0)	249.4	255.0	–	–
(9,0)	253.9	–	269.0	357.0
(14,0)	258.3	–	–	362.0

Table 14 E_z (N/m) of SiCNTs compared with the literature

SiCNTs	E_z	[34]
(4,4)	151.5	157.0
(5,5)	153.2	162.0
(8,8)	155.1	166.0
(5,0)	142.7	143.0
(9,0)	151.3	160.0

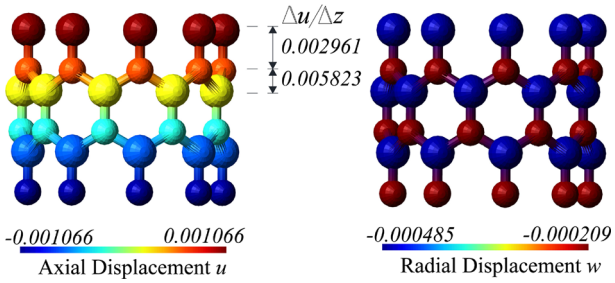

Fig. 11 (9,0) BNNT: displacements under axial loads

In conclusion, the procedure adopted is very simple, even in regard to a possible analytical evaluation of the elastic constants. Also in view of an augmented Cauchy–Born kinematic map, it is worth highlighting that periodic deformations of the diatomic nanotubes can be seen as the superimposition of the homogeneous deformation of a cylindrical shell and some small-scale contributions. Figures 11, 12, 13, 14, 15 and 16 show the displacements of some innermost atom rows of (9,0) and (5,5) BNNTs, respectively.

More precisely, for the zigzag case, the two slopes $\Delta u/\Delta z$ (see Figs. 11 and 12) and $\Delta v/\Delta z$ (see Fig. 13) suggest two different local axial and shear strains, which can be obtained by summing an average displacement to two opposite axial or circumferential displacements for each couple of first neighbours. Also for the armchair case, opposite circumferential (see Figs. 14 and 15) and axial (see Fig. 16) displacements for any two first neighbours arise and in this case they imply local non-uniform shear and circumferential strains. The interested reader is referred to [78] for more details.

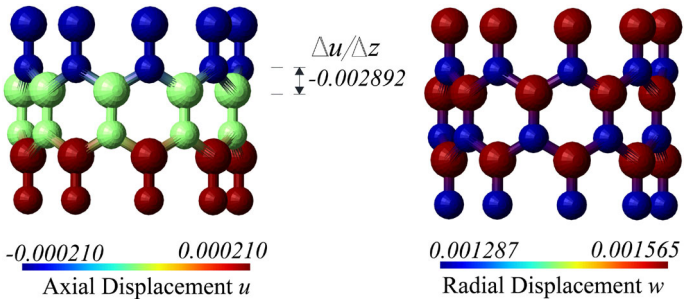

Fig. 12 (9,0) BNNT: displacements under radial loads

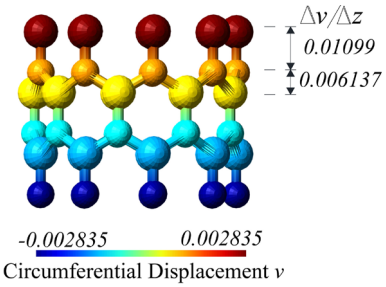

Fig. 13 (9,0) BNNT: displacements under torsional loads

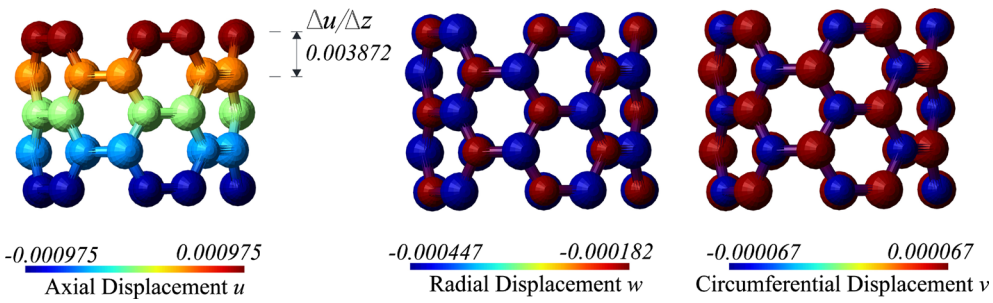

Fig. 14 (5,5) BNNT: displacements under axial loads

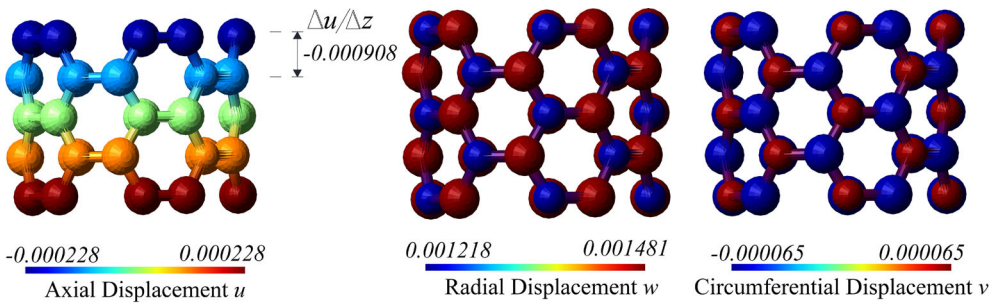

Fig. 15 (5,5) BNNT: displacements under radial loads

In addition to these effects, common to CNTs, in tensile and radial tests of the diatomic nanotubes, we find two different radial displacements for the atoms of type 1 and 2, as a consequence of the diversification of the angular force constants. This suggests a mean radial displacement accompanied by opposite radial displacements for each couple of first neighbours.

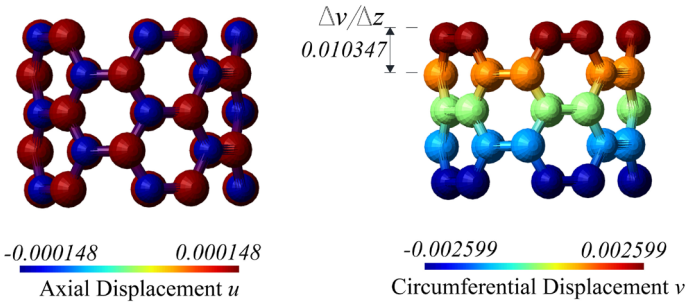

Fig. 16 (5,5) BNNT: displacements under torsional loads

6 Conclusions

In this paper, a numerical study of the nanoscale mechanical behaviour of defect-free single-wall CNTs, BNNTs and SiCNTs has been carried out, using a stick-and-spring model based on Morse and cosine energy functions. The relaxed configuration of the tubes has been evaluated, and tensile, torsional and radial tests have been performed.

Due to the negligible differences in terms of length and of radius between the ideal and the relaxed configurations, a Donnell thin shell model, assumed equivalent to the ideal nanotube, has been used for a comprehensive evaluation of the elastic constants.

Comparisons with the available ab-initio results have been addressed. In the case of SiC hexagonal nanomaterials, a set of parameters, well suited to reproduce the relaxed configurations and the elastic constants, has been established.

The numerical results obtained in this work have shown the non-isotropic behaviour of BNNTs and SiCNTs. Furthermore, the good results provided by nonlinear analyses performed in order to obtain the relaxed configuration encourage us to exploit the simplest interatomic potentials also in highly nonlinear analyses, where ab-initio simulations become impracticable.

Finally, a focus on the small-scale effects has been provided. Obviously, these effects cannot be represented by a Donnell thin shell model because it captures only the average behaviour of the tube. Therefore, recourse to non-standard continuum models is needed when small-scale effects become relevant.

In the literature, some modified beam models, endowed with scale parameters, have been identified for the analysis of CNTs [100,101], while for BNNTs and SiCNTs non-standard continuum models are still lacking. It is our belief that the small-scale effects seen for armchair nanotubes could reasonably be reproduced also by complementing the standard kinematics of a beam with proper deformation modes of the cross sections, similarly to what has been done several times, also in the nonlinear range, in the context of profiles with thin-walled and/or composite sections (e.g. [102,103]).

Acknowledgements We are very grateful to the University "Roma Tre" for cofunding the research contract of Ph.D. Alessandra Genoese and to the Italian Ministry of University, Research and Education for cofunding the research contract of Ph.D. Andrea Genoese.

Compliance with ethical standards

Conflict of interest

The authors declare that they have no conflict of interest.

Appendix: The iteration matrix

To compute the iteration matrix, we perform the first variation with respect to the displacements of the force vectors in Eq. (13b). Starting from $\boldsymbol{f}_{ij}$ and recalling Eq. (6a), we have

$$\frac{\partial \boldsymbol{f}_{ij}}{\partial \boldsymbol{u}_{ij}}\delta\boldsymbol{u}_{ij} = \left[k_{ij}\,\boldsymbol{i}_{ij}\left(\frac{\partial r_{ij}}{\partial \boldsymbol{u}_{ij}}\right)\cdot\delta\boldsymbol{u}_{ij} + f_{ij}\,\frac{\partial \boldsymbol{i}_{ij}}{\partial \boldsymbol{u}_{ij}}\delta\boldsymbol{u}_{ij}\right]. \tag{24}$$

Then, by substituting Eq. (10), we obtain

$$\frac{\partial \boldsymbol{f}_{ij}}{\partial \boldsymbol{u}_{ij}} = \left(k_{ij} - \frac{f_{ij}}{r_{ij}}\right) \boldsymbol{i}_{ij} \otimes \boldsymbol{i}_{ij} + \frac{f_{ij}}{r_{ij}} \boldsymbol{I}.$$

Before differentiating $\boldsymbol{t}_{ij}$ and $\boldsymbol{t}_{ik}$, it is convenient to identify the pair of sticks i–j and i–k through the indices $\alpha, \beta, \gamma \in \{ij,\ ik\}$, with $\gamma \neq \alpha$. Recalling Eqs. (6b) and (13b), we obtain

$$\frac{\partial \boldsymbol{t}_{\alpha}}{\partial \boldsymbol{u}_{\beta}} \delta \boldsymbol{u}_{\beta} = \left[\frac{k_{ijk}}{r_{\alpha}} \boldsymbol{n}_{\alpha} \left(\frac{\partial \theta_{ijk}}{\partial \boldsymbol{u}_{\beta}} \right) \cdot \delta \boldsymbol{u}_{\beta} + m_{ijk} \frac{\partial}{\partial \boldsymbol{u}_{\beta}} \left(\frac{\boldsymbol{n}_{\alpha}}{r_{\alpha}} \right) \delta \boldsymbol{u}_{\beta} \right]. \tag{25}$$

By taking into account Eqs. (10) and (11), it also follows that

$$\begin{aligned}
\frac{\partial}{\partial \boldsymbol{u}_{\alpha}} \left(\frac{\boldsymbol{n}_{\alpha}}{r_{\alpha}} \right) \delta \boldsymbol{u}_{\alpha} &= \frac{\mathrm{d}}{\mathrm{d}r_{\alpha}} \left(\frac{1}{r_{\alpha}} \right) \left[\left(\frac{\partial r_{\alpha}}{\partial \boldsymbol{u}_{\alpha}} \right) \cdot \delta \boldsymbol{u}_{\alpha} \right] \boldsymbol{n}_{\alpha} + \frac{1}{r_{\alpha}} \frac{\partial \boldsymbol{n}_{\alpha}}{\partial \boldsymbol{u}_{\alpha}} \delta \boldsymbol{u}_{\alpha} \\
&= -\frac{1}{r_{\alpha}^2} (\boldsymbol{n}_{\alpha} \otimes \boldsymbol{i}_{\alpha}) \delta \boldsymbol{u}_{\alpha} + \frac{1}{r_{\alpha}} \frac{\cos \theta_{ijk}}{\sin \theta_{ijk}} \frac{\partial \boldsymbol{i}_{\alpha}}{\partial \boldsymbol{u}_{\alpha}} \delta \boldsymbol{u}_{\alpha} \\
&\quad - \frac{1}{r_{\alpha}} \left(\frac{\cos \theta_{ijk}}{\sin \theta_{ijk}} \boldsymbol{n}_{\alpha} + \boldsymbol{i}_{\alpha} \right) \left(\frac{\partial \theta_{ijk}}{\partial \boldsymbol{u}_{\alpha}} \right) \cdot \delta \boldsymbol{u}_{\alpha} \\
&= \frac{1}{r_{\alpha}^2 \sin \theta_{ijk}} \left[\cos \theta_{ijk} \left(\boldsymbol{I} - 3 \boldsymbol{i}_{\alpha} \otimes \boldsymbol{i}_{\alpha} - \boldsymbol{n}_{\alpha} \otimes \boldsymbol{n}_{\alpha} \right) \right. \\
&\quad \left. + \boldsymbol{i}_{\alpha} \otimes \boldsymbol{i}_{\gamma} + \boldsymbol{i}_{\gamma} \otimes \boldsymbol{i}_{\alpha} \right] \delta \boldsymbol{u}_{\alpha},
\end{aligned} \tag{26a}$$

$$\begin{aligned}
\frac{\partial \boldsymbol{n}_{\alpha}}{\partial \boldsymbol{u}_{\gamma}} \delta \boldsymbol{u}_{\gamma} &= -\frac{1}{\sin \theta_{ijk}} \frac{\partial \boldsymbol{i}_{\gamma}}{\partial \boldsymbol{u}_{\gamma}} \delta \boldsymbol{u}_{\gamma} - \left(\frac{\cos \theta_{ijk}}{\sin \theta_{ijk}} \boldsymbol{n}_{\alpha} + \boldsymbol{i}_{\alpha} \right) \left(\frac{\partial \theta_{ijk}}{\partial \boldsymbol{u}_{\gamma}} \right) \cdot \delta \boldsymbol{u}_{\gamma} \\
&= \frac{1}{r_{\gamma} \sin \theta_{ijk}} \left[\boldsymbol{i}_{\alpha} \otimes \boldsymbol{i}_{\alpha} + \boldsymbol{i}_{\gamma} \otimes \boldsymbol{i}_{\gamma} - \boldsymbol{I} \right. \\
&\quad \left. - \cos \theta_{ijk} (\boldsymbol{i}_{\alpha} \otimes \boldsymbol{i}_{\gamma} + \boldsymbol{n}_{\alpha} \otimes \boldsymbol{n}_{\gamma}) \right] \delta \boldsymbol{u}_{\gamma}.
\end{aligned} \tag{26b}$$

Then, substituting (26) into Eq. (25) and recalling Eq. (11), we obtain

$$\begin{aligned}
\frac{\partial \boldsymbol{t}_{\alpha}}{\partial \boldsymbol{u}_{\alpha}} &= \frac{1}{r_{\alpha}^2} \left\{ \left(k_{ijk} - \frac{m_{ijk}}{\tan \theta_{ijk}} \right) \boldsymbol{N}_{\alpha\alpha} + \frac{m_{ijk}}{\sin \theta_{ijk}} \left[\cos \theta_{ijk} \left(\boldsymbol{I} - 3 \boldsymbol{I}_{\alpha\alpha} \right) + \boldsymbol{I}_{\alpha\gamma} + \boldsymbol{I}_{\gamma\alpha} \right] \right\}, \\
\frac{\partial \boldsymbol{t}_{\alpha}}{\partial \boldsymbol{u}_{\gamma}} &= \frac{1}{r_{\alpha} r_{\gamma}} \left[\left(k_{ijk} - \frac{m_{ijk}}{\tan \theta_{ijk}} \right) \boldsymbol{N}_{\alpha\gamma} + \frac{m_{ijk}}{\sin \theta_{ijk}} \left(\boldsymbol{I}_{\alpha\alpha} + \boldsymbol{I}_{\gamma\gamma} - \boldsymbol{I} - \cos \theta_{ijk} \boldsymbol{I}_{\alpha\gamma} \right) \right],
\end{aligned}$$

where $\boldsymbol{N}_{\alpha\beta} = \boldsymbol{n}_{\alpha} \otimes \boldsymbol{n}_{\beta}$ and $\boldsymbol{I}_{\alpha\beta} = \boldsymbol{i}_{\alpha} \otimes \boldsymbol{i}_{\beta}$. Finally, in the linear case, this reduces to

$$\frac{\partial \boldsymbol{f}_{ij}}{\partial \boldsymbol{u}_{ij}} = \tilde{k}_{ij} \tilde{\boldsymbol{i}}_{ij} \otimes \tilde{\boldsymbol{i}}_{ij}, \quad \frac{\partial \boldsymbol{t}_{\alpha}}{\partial \boldsymbol{u}_{\beta}} = \frac{\tilde{k}_{ijk}}{\tilde{r}_{\alpha} \tilde{r}_{\beta}} \tilde{\boldsymbol{n}}_{\alpha} \otimes \tilde{\boldsymbol{n}}_{\beta}.$$

References

1. Choi, W., Lahiri, I., Seelaboyina, R., Kang, Y.S.: Synthesis of graphene and its applications: a review. Crit. Rev. Solid State Mater. Sci. **35**, 52–71 (2010)
2. De Volder, M.F.L., Tawfick, S.H., Baughman, R.H., Hart, A.J.: Carbon nanotubes: present and future commercial applications. Science **339**, 535–539 (2013)
3. Sun, C., Wen, B., Bai, B.: Recent advances in nanoporous graphene membrane for gas separation and water purification. Sci. Bull. **60**, 1807–1823 (2015)
4. Nguyen, B.H., Nguyen, V.H.: Promising applications of graphene and graphene-based nanostructures. Adv. Nat. Sci. Nanosci. Nanotechnol. **7**, 023002 (2016)
5. Ates, M., Eker, A.A., Eker, B.: Carbon nanotube-based nanocomposites and their applications. J. Adhes. Sci. Technol. **31**, 1977–1997 (2017)
6. Kumar, R., Singh, R., Hui, D., Feo, L., Fraternali, F.: Graphene as biomedical sensing element: state of art review and potential engineering applications. Compos. B Eng. **134**, 193–206 (2018)

7. Mohan, V.B., Lau, K.-T., Hui, D., Bhattacharyya, D.: Graphene-based materials and their composites: a review on production, applications and product limitations. Compos. B Eng. **142**, 200–220 (2018)
8. Chopra, N.G., Luyken, R.J., Cherry, K., Crespi, V.H., Cohen, M.L., Louie, S.G., et al.: Boron nitride nanotubes. Science **269**, 966–967 (1995)
9. Sun, X.H., Li, C.P., Wong, W.K., Wong, N.B., Lee, C.S., Lee, S.T., et al.: Formation of silicon carbide nanotubes and nanowires via reaction of silicon (from disproportionation of silicon monoxide) with carbon nanotubes. J. Am. Chem. Soc. **124**, 14464–14471 (2002)
10. Pacilé, D., Meyer, J.C., Girit, Ç.Ö., Zettl, A.: The two-dimensional phase of boron nitride: few-atomic-layer sheets and suspended membrane. Appl. Phys. Lett. **92**, 133107 (2008)
11. Song, L., Ci, L., Lu, H., Sorokin, P.B., Jin, C., Ni, J., et al.: Large scale growth and characterization of atomic hexagonal boron nitride layers. Nano Lett. **10**, 3209–3215 (2010)
12. Lin, S.S.: Light-emitting two-dimensional ultrathin silicon carbide. J. Phys. Chem. C **116**, 3951–3955 (2012)
13. Casady, J.B., Johnson, R.W.: Status of silicon carbide (SiC) as a wide-bandgap semiconductor for high temperature applications: a review. Solid State Electron. **39**, 1409–1422 (1996)
14. Suryavanshi, A.P., Yu, M.F., Wen, J., Tang, C., Bando, Y.: Elastic modulus and resonance behavior of boron nitride nanotubes. Appl. Phys. Lett. **84**, 2527 (2004)
15. Falin, A., Cai, Q., Santos, E.J.G., Scullion, D., Qian, D., Zhang, R., et al.: Mechanical properties of atomically thin boron nitride and the role of interlayer interactions. Nat. Commun. **8**, 15815 (2017)
16. Ouyang, T., Chen, Y., Xie, Y., Yang, K., Bao, Z., Zhong, J.: Thermal transport in hexagonal boron nitride nanoribbons. Nanotechnology **21**, 245701 (2010)
17. Golberg, D., Bando, Y., Huang, Y., Terao, T., Mitome, M., Tang, C., et al.: Boron nitride nanotubes and nanosheets. ACS Nano **4**, 2979–2993 (2010)
18. Kakay, S., Yilmaz, Z., Sen, O., Emanet, M., Kazanc, E., Çulha, M.: Synthesis of boron nitride nanotubes and their applications. Beilstein J. Nanotechnol. **6**, 84–102 (2015)
19. Kumar, R., Parashar, A.: Atomistic modeling of BN nanofillers for mechanical and thermal properties: a review. Nanoscale **8**, 22–49 (2016)
20. Li, Q., Liu, M., Zhang, Y., Liu, Z.: Hexagonal boron nitride–graphene heterostructures: synthesis and interfacial properties. Small **12**, 32–50 (2016)
21. Mpourmpakis, G., Froudakis, G.E., Lithoxoos, G.P., Samios, J.: SiC nanotubes: a novel material for hydrogen storage. Nano Lett. **6**, 1581–1583 (2006)
22. Zhang, G., Zhang, Y.-W.: Strain effects on thermoelectric properties of two-dimensional materials. Mech. Mater. **91**, 382–398 (2015)
23. Shima, H.: Buckling of carbon nanotubes: a state of art review. Materials **5**, 47–84 (2012)
24. Akinwande, D., Brennan, C.J., Scott Bunch, J., Egberts, P., Felts, J.R., Gao, H., et al.: A review on mechanics and mechanical properties of 2D materials-graphene and beyond. Extreme Mech. Lett. **13**, 42–77 (2017)
25. Krishnan, A., Dujardin, E., Ebbesen, T.W., Yianilos, P.N., Treacy, M.M.J.: Young's modulus of single-walled nanotubes. Phys. Rev. B **58**, 14013–14019 (1998)
26. Sánchez-Portal, D., Artacho, E., Soler, J.M., Rubio, A., Ordejón, P.: Ab-initio structural, elastic, and vibrational properties of carbon nanotubes. Phys. Rev. B **59**, 678–688 (1999)
27. Kudin, K.N., Scuseria, G.E., Yakobson, B.I.: C_2F, BN, and C nanoshell elasticity from ab-initio computations. Phys. Rev. B **64**, 235406 (2001)
28. Machón, M., Reich, S., Thomsen, C., Sánchez-Portal, D., Ordejón, P.: Ab-initio calculations of the optical properties of 4-Å-diameter single-walled nanotubes. Phys. Rev. B **66**, 155410–5 (2002)
29. Cabria, I., Mintmire, J.W., White, C.T.: Metallic and semiconducting narrow carbon nanotubes. Phys. Rev. B **67**, 121406(R) (2003)
30. Popov, V.N.: Curvature effects on the structural, electronic and optical properties of isolated single-walled nanotubes within a symmetry-adapted non-orthogonal tight-binding model. New J. Phys. **6**, 1–18 (2004)
31. Bogár, F., Mintmire, J.W., Bartha, F., Mezö, T., Van Alsenoy, C.: Density-functional study of the mechanical and electronic properties of narrow carbon nanotubes under axial stress. Phys. Rev. B **72**, 085452 (2005)
32. Jia, J.-F., Wu, H.-S., Jiao, H.: The structure and electronic property of BN nanotube. Physica B **381**, 90–95 (2006)
33. Zhao, M., Xia, Y., Li, F., Zhang, R.Q., Lee, S.-T.: Strain energy and electronic structures of silicon carbide nanotubes: density functional calculations. Phys. Rev. B **71**, 085312 (2005)
34. Baumeier, B., Krüger, P., Pollmann, J.: Structural, elastic, and electronic properties of SiC, BN, and BeO nanotubes. Phys. Rev. B **76**, 085407 (2007)
35. Alam, K.M., Ray, A.K.: Hybrid density functional study of armchair SiC nanotubes. Phys. Rev. B **77**, 035436 (2008)
36. Şahin, H., Cahangirov, S., Topsakal, M., Bekaroglu, E., Akturk, E., Senger, R.T., et al.: Monolayer honeycomb structures of group-IV elements and III–V binary compounds: first-principles calculations. Phys. Rev. B **80**, 155453 (2009)
37. Domínguez-Rodríguez, G.: An assessment of finite element analysis to predict the elastic modulus and Poisson's ratio of single wall carbon nanotubes. Comput. Mater. Sci. **82**, 257–263 (2014)
38. Chandraseker, K., Mukherjee, S.: Atomistic-continuum and ab-initio estimation of the elastic moduli of single-walled carbon nanotubes. Comput. Mater. Sci. **40**, 147–158 (2007)
39. Hung, N.T., Truong, D.V., Thanh, V.V., Saito, R.: Intrinsic strength and failure behaviors of ultra-small single-walled carbon nanotubes. Comput. Mater. Sci. **114**, 167–171 (2016)
40. Peng, Y.-J., Zhang, L.-Y., Jin, Q.-H., Li, B.-H., Ding, D.-T.: Ab-initio studies of elastic properties and electronic structures of C and BN nanotubes. Physica E **33**, 155–159 (2006)
41. Chang, T., Gao, H.: Size-dependent elastic properties of a single-walled carbon nanotube via a molecular mechanics model. J. Mech. Phys. Solids **51**, 1059–1074 (2003)
42. Meo, M., Rossi, M.: Prediction of Young's modulus of single wall carbon nanotubes by molecular-mechanics based finite element modelling. Compos. Sci. Technol. **66**, 1597–1605 (2006)

43. Verma, V., Jindal, V.K., Dharamvir, K.: Elastic moduli of a boron nitride nanotube. Nanotechnology **18**, 435711 (2007)
44. Jindal, V.K., Imtani, A.N.: Bond lengths of armchair single-walled carbon nanotubes and their pressure dependence. Comput. Mater. Sci. **44**, 156–162 (2008)
45. Meo, M., Rossi, M.: On the estimation of mechanical properties of single-walled carbon nanotubes by using a molecular-mechanics based FE approach. Compos. Sci. Technol. **69**, 1394–1398 (2009)
46. Xiao, J.R., Staniszewski, J., Gillespie Jr., J.W.: Fracture and progressive failure of defective graphene sheets and carbon nanotubes. Compos. Struct. **88**, 602–609 (2009)
47. Wernik, J.M., Meguid, S.A.: Atomistic-based continuum modeling of the nonlinear behavior of carbon nanotubes. Acta Mech. **212**, 167–179 (2010)
48. Berinskii, I.E., Krivtsov, A.M.: On using many-particle interatomic potentials to compute elastic properties of graphene and diamonds. Mech. Solut. **45**, 815–883 (2010)
49. Oh, E.-S.: Elastic properties of boron-nitride nanotubes through the continuum lattice approach. Mater. Lett. **64**, 859–862 (2010)
50. Jiang, L., Guo, W.: A molecular mechanics study on size-dependent elastic properties of single-walled boron nitride nanotubes. J. Mech. Phys. Solids **59**, 1204–1213 (2011)
51. Oh, E.-S.: Elastic properties of various boron-nitride structures. Met. Mater. Int. **17**, 21–27 (2011)
52. Parvaneh, V., Shariati, M.: Effect of defects and loading on prediction of Young's modulus of SWCNTs. Acta Mech. **216**, 281–289 (2011)
53. Silvestre, N., Faria, B., Canongia Lopes, J.N.: A molecular dynamics study on the thickness and post-critical strength of carbon nanotubes. Compos. Struct. **94**, 1352–1358 (2012)
54. Ansari, R., Mirnezhad, M., Sahmani, S.: An accurate molecular mechanics model for computation of size-dependent elastic properties of armchair and zigzag single-walled carbon nanotubes. Meccanica **48**, 1355–1367 (2013)
55. Berinskii, I.E., Borodich, F.M.: Elastic in-plane properties of 2D linearized models of graphene. Mech. Mater. **62**, 60–68 (2013)
56. Davini, C.: Homogenization of a graphene sheet. Contin. Mech. Thermodyn. **26**, 95–113 (2014)
57. Korobeynikov, S.N., Alyokhin, V.V., Babichev, A.V.: Application of the molecular mechanics method to simulation of buckling of single-walled carbon nanotubes. Eng. Fract. Mech. **130**, 83–95 (2014)
58. Le, M.-Q.: Atomistic study on the tensile properties of hexagonal AlN, BN, GaN, InN and SiC sheets. J. Comput. Theor. Nanosci. **11**, 1458–1464 (2014)
59. Le, M.-Q., Nguyen, D.-T.: Atomistic simulations of pristine and defective hexagonal BN and SiC sheets under uniaxial tension. Mater. Sci. Eng. A **615**, 481–488 (2014)
60. Le, M.-Q.: Young's modulus prediction of hexagonal nanosheets and nanotubes based on dimensional analysis and atomistic simulations. Meccanica **49**, 1709–1719 (2014)
61. Le, M.-Q.: Prediction of the Young's modulus of hexagonal monolayer sheets based on molecular mechanics. Int. J. Mech. Mater. Des. **11**, 15–24 (2015)
62. Korobeynikov, S.N., Alyokhin, V.V., Annin, B.D., Babichev, A.V.: Quasi-static buckling simulation of single-layer graphene sheets by the molecular mechanics method. Math. Mech. Solids **20**, 836–870 (2015)
63. Gamboa, A., Vignoles, G.L., Leyssale, J.-M.: On the prediction of graphene's elastic properties with reactive empirical bond order potential. Carbon **89**, 176–187 (2015)
64. Tao, J., Xu, G., Sun, Y.: Elastic properties of boron-nitride nanotubes through an atomic simulation method. Math. Probl. Eng. **2015**, 240547 (2015)
65. Yan, J.W., Liew, K.M.: Predicting elastic properties of single-walled boron nitride nanotubes and nanocones using an atomistic-continuum approach. Compos. Struct. **125**, 489–498 (2015)
66. Favata, A., Micheletti, A., Podio-Guidugli, P., Pugno, N.: Geometry and self-stress of single-wall carbon nanotubes and graphene via a discrete model based on a 2nd-generation REBO potential. J. Elast. **125**, 1–37 (2016)
67. Genoese, A., Genoese, A., Rizzi, N.L., Salerno, G.: On the derivation of the elastic properties of lattice nanostructures: the case of graphene sheets. Compos. B Eng. **115**, 316–329 (2017)
68. Merli, R., Lázaro, C., Monleón, S., Domingo, A.: Energy approach to the unstressed geometry of single walled carbon nanotubes. Meccanica **52**, 213–230 (2017)
69. Lee, H.-L., Wang, S.-W., Yang, Y.-C., Chang, W.-J.: Effect of porosity on the mechanical properties of a nanoporous graphene membrane using the atomic-scale finite element method. Acta Mech. **228**, 2623–2629 (2017)
70. Budarapu, P.R., Javvaji, B., Sutrakar, V.K., Roy Mahapatra, D., Paggi, M., Zi, G., Rabczuk, T.: Lattice orientation and crack size effect on the mechanical properties of Graphene. Int. J. Fract. **203**, 81–98 (2017)
71. Li, N., Ding, N., Qu, S., Liu, L., Guo, W., Wu, C.-H.L.: Mechanical properties and failure behavior of hexagonal boron nitride sheets with nano-cracks. Comput. Mater. Sci. **140**, 356–366 (2017)
72. Natsuki, T., Natsuki, J.: Prediction of mechanical properties for hexagonal boron nitride nanosheets using molecular mechanics model. Appl. Phys. A **123**, 283 (2017)
73. Tapia, A., Cab, C., Hernández-Pérez, A., Villanueva, C., Peñuñuri, F., Avilés, F.: The bond force constants and elastic properties of boron nitride nanosheets and nanoribbons using a hierarchical modelling approach. Physica E **89**, 183–193 (2017)
74. Genoese, A., Genoese, A., Rizzi, N.L., Salerno, G.: Force constants of BN, SiC, AlN and GaN sheets through discrete homogenization. Meccanica **53**, 593–611 (2018)
75. Hossain, M.Z., Hao, T., Silverman, B.: Stillinger-Weber potential for elastic and fracture properties in graphene and carbon nanotubes. J. Phys. Condens. Matter. **30**, 055901 (2018)
76. Vijayaraghavan, V., Zhang, L.: Effective mechanical properties and thickness determination of boron nitride nanosheets using molecular dynamics simulation. Nanomaterials **8**, 546 (2018)
77. Korobeynikov, S.N., Alyokhin, V.V., Babichev, A.V.: Simulation of mechanical parameters of graphene using the DREIDING force field. Acta Mech. **229**, 2343–2378 (2018)

78. Genoese, A., Genoese, A., Salerno, G.: Elastic constants of achiral single-wall CNTs: analytical expressions and a focus on size and small scale effects. Compos. B Eng. **147**, 207–226 (2018)
79. Wan, H., Delale, F.: A structural mechanics approach for predicting the mechanical properties of carbon nanotubes. Meccanica **45**, 43–51 (2010)
80. Tserpes, K.I.: Strength of graphenes containing randomly dispersed vacancies. Acta Mech. **223**, 669–678 (2012)
81. Torabi, H., Shariati, M., Sedaghat, E., Zadeh, A.L.: Buckling behavior of perfect and defective DWCNTs under axial, bending and torsional loadings via a structural mechanics approach. Meccanica **48**, 1959–1974 (2013)
82. Sakharova, N.A., Pereira, A.F.G., Antunes, J.M., Brett, C.M.A., Fernandes, J.V.: Mechanical characterization of single-walled carbon nanotubes: numerical simulation study. Compos. B Eng. **75**, 73–85 (2015)
83. Giannopoulos, G.I., Kontoni, D.-P.N., Georgantzinos, S.K.: Efficient FEM simulation of static and free vibration behavior of single walled boron nitride nanotubes. Superlattice Microstruct. **96**, 111–120 (2016)
84. Rafiee, R., Eskandariyun, A.: Comparative study on predicting Young's modulus of graphene sheets using nano-scale continuum mechanics approach. Physica E **90**, 42–48 (2017)
85. Giannopoulos, G.I.: On the buckling of hexagonal boron nitride nanoribbons via structural mechanics. Superlattices Microstruct. **115**, 1–9 (2018)
86. Silvestre, N., Wang, C.M., Zhang, Y.Y., Xiang, Y.: Sanders shell model for buckling of single-walled carbon nanotubes with small aspect ratio. Compos. Struct. **93**, 1683–1691 (2011)
87. Silvestre, N.: On the accuracy of shell models for torsional buckling of carbon nanotubes. Eur. J. Mech. A Solids **32**, 103–108 (2012)
88. Hollerer, S., Celigoj, C.C.: Buckling analysis of carbon nanotubes by a mixed atomistic and continuum model. Comput. Mech. **51**, 765–789 (2013)
89. Allahbakhshi, A., Allahbakhshi, M.: Vibration analysis of nano-structure multilayered graphene sheets using modified strain gradient theory. Front. Mech. Eng. **10**, 187–197 (2015)
90. Fadaee, M., Ilkhani, M.R.: Study on the effect of an eccentric hole on the vibrational behavior of a graphene sheet using an analytical approach. Acta Mech. **226**, 1395–1407 (2015)
91. Aminpour, H., Rizzi, N.L.: A one-dimensional continuum with microstructure for single-wall carbon nanotubes bifurcation analysis. Math. Mech. Solids **21**, 168–181 (2016)
92. Jandaghian, A.A., Rahmani, O.: Buckling analysis of multi-layered graphene sheets based on a continuum mechanics model. Appl. Phys. A **123**, 324 (2017)
93. Sahmani, S., Fattahi, A.M.: Development of efficient size-dependent plate models for axial buckling of single-layered graphene nanosheets using molecular dynamics simulation. Microsyst. Technol. **24**, 1265–1277 (2018)
94. Singh, S., Patel, B.P.: A computationally efficient multiscale finite element formulation for dynamic and postbuckling analyses of carbon nanotubes. Comput. Struct. **195**, 126–144 (2018)
95. Erhart, P., Albe, K.: Analytical potential for atomistic simulations of silicon, carbon and silicon carbide. Phys. Rev. B **71**, 035211 (2005)
96. Rappé, A.K., Casewit, C.J., Colwell, K.S., Goddardlll, W.A., Skiff, W.M.: UFF, a full periodic table force field for molecular mechanics and molecular dynamics simulations. J. Am. Chem. Soc. **114**, 10024–10035 (1992)
97. Donnell, L. H.: Stability of Thin-Walled Tubes Under Torsion. NACA 479 (1935)
98. Geuzaine, C., Remacle, J.-F.: Gmsh: a three-dimensional finite element mesh generator with built-in pre- and post-processing facilities. Int. J. Numer. Methods Eng. **79**, 1309–1331 (2009)
99. Nozaki, H., Itoh, S.: Structural stability of BC_2N. J. Phys. Chem. Solids **57**, 41–49 (1996)
100. Malagù, M., Benvenuti, E., Simone, A.: One-dimensional nonlocal elasticity for tensile single-walled carbon nanotubes: a molecular structural mechanics characterization. Eur. J. Mech. A Solids **54**, 160–170 (2015)
101. Barretta, R., Brčić, M., Čanađija, M., Luciano, R., Marotti-de-Sciarra, F.: Application of gradient elasticity to armchair carbon nanotubes: size effects and constitutive parameters assessment. Eur. J. Mech. A Solids **65**, 1–13 (2017)
102. Genoese, A., Genoese, A., Bilotta, A., Garcea, G.: Buckling analysis through a generalized beam model including section distortions. Thin Walled Struct. **85**, 125–141 (2014)
103. Gabriele, S., Rizzi, N.L., Varano, V.: A 1D nonlinear TWB model accounting for in plane cross-section deformation. Int. J. Solids Struct. **94–95**, 170–178 (2016)